5-2024

Oxider to Fuel Ratio Shift Compensation Via Vortex Strength Control in Hybrid Rocket Motors

Max W. Francom
Utah State University, a02219655@usu.edu

OXIDER TO FUEL RATIO SHIFT COMPENSATION VIA VORTEX STRENGTH CONTROL IN HYBRID ROCKET MOTORS

by

Max W. Francom

A thesis submitted in partial fulfillment

of the requirements for the degree

of

MASTER OF SCIENCE

in

Aerospace Engineering

Approved:

_____	_____
Stephen A. Whitmore, Ph.D. Major professor	Ryan Berke, Ph.D. Committee member
_____	_____
Som Dutta, Ph.D. Committee member	D. Richard Cutler, Ph.D. Vice Provost of Graduate Studies

UTAH STATE UNIVERSITY
Logan, Utah

2024

ABSTRACT

Oxidizer to Fuel Ratio Shift Compensation Via Vortex Strength Control in Hybrid Rocket Motors

by

Max Francom

Utah State University, 2024

Major Professor: Dr. Stephen A. Whitmore
Department: Mechanical and Aerospace Engineering

Hybrid motors have existed as a hypothetical propulsion system for decades in a wide range of upper stage rocket motors due to their simple, robust, non-toxic, and versatile nature. However, inherent to hybrids is Oxidizer to Fuel ratio (O/F) shift over time, the result of which is non-optimal performance for the majority of the rocket's lifetime. One potential method of O/F manipulation is achieved by controlling the vorticity of combustion gasses via oxidizer injection. This thesis presents a controllable vortex motor and evaluates the effectiveness of vortex strength control in compensating for the motor's natural O/F shift. The 98mm gaseous oxygen (GOX)-ABS motor utilizes USU's previously-developed hybrid rocket systems and test infrastructure. Performance data has been analyzed and compared with analytical and numerical models and then used to develop a control scheme to compensate for O/F shift. The performance of the O/F compensating motor is discussed, and the data compared with expected combustion behavior.

(68 Pages)

PUBLIC ABSTRACT

Oxidizer to Fuel Ratio Shift Compensation Via Vortex Strength Control in Hybrid Rocket Motors

Max Francom

Hybrid motors have existed as a hypothetical propulsion system for decades in a wide range of upper stage rocket motors due to their simple, robust, non-toxic, and versatile nature. However, inherent to hybrids is Oxidizer to Fuel ratio (O/F) shift over time, which results in performance losses for the majority of the rocket's lifetime. The purpose of this study is to develop a hybrid rocket motor capable of manipulating O/F at will, resulting in an engine which eliminates the undesirable effects of O/F shift. By developing and refining a numerical simulation, a novel injector system, and an open-loop control scheme, this thesis demonstrates programmable O/F manipulation in an experimental hybrid engine.

ACKNOWLEDGMENTS

Thank you to Dr. Stephen Whitmore for essential mentorship and guidance, my colleagues Trevor Coombs, Cara Borealis, Ryan Thibaudeau, and Terry Zollinger at the USU Experimental Rocketry and Propulsion Research Laboratory for their support, my Heavenly Father, and my wife, Olivia, who motivates everything I do.

Max Francom

CONTENTS

Page

LIST OF TABLES

Page

LIST OF FIGURES

Page

SYMBOLS

$\dot{r}$	Fuel Regression Rate
c*	Characteristic Velocity
η^*	Efficiency
Isp	Specific Impulse
ρ	Density
μ	Dynamic Viscosity
x	Position Along Fuel Grain Axis
G	Mass Flux
B	Blowing Coefficient
P_r	Prandtl Number
a	Burn Coefficient
n	Burn Exponent
S_g	Swirl Number
$\dot{m}$	Massflow Rate
t	Time
d	Diameter
D	Feed Diameter
A_{Cf}	Skin Friction Coefficient
A_β	Blowing Suppression Coefficient
M_W	Molecular Weight

r	radius
V_{ratio}	Vortex Strength Ratio
m	Burn Length Exponent/Secondary Burn Exponent
C_d	Discharge Coefficient
P_0	Stagnation Pressure/Chamber Pressure
A	Area
γ	Specific Heat/Gamma
R_g	Specific Gas Constant
T_0	Stagnation Temperature/Flame Temperature
Re	Reynold's Number
C_v	Volumetric Flow Coefficient
F	Thrust
P	Pressure
V	Voltage
I	Current
m	Mass
M	Mach Number
V_{exit}	Exit Velocity
I_{total}	Impulse

ACRONYMS

O/F	Oxidizer-to-Fuel Ratio
ABS	Acrylonitrile Butadiene Styrene
GOX	Gaseous Oxygen
USU	Utah State University
NASA	National Aeronautics and Space Administration
MSFC	Marshall Spaceflight Center
CEA	Chemical Equilibrium with Applications
JAXA	Japan Aerospace Exploration Agency

CHAPTER 1

INTRODUCTION

1.1 Background and Motivation

Hybrid rocketry has been extensively researched by USU's Propulsion Research Laboratory since 2008. As a result, USU has expertise, infrastructure, and technology readily available to research and develop new hybrid motors. This project builds on previous work performed by the propulsion lab, including USU's 98mm GOX-ABS motor, the lab's low-energy 3D-printed ignition system, and non-invasive spectroscopy of rocket combustion chambers.

Hybrid rocket motors offer a wide range of potential benefits to spaceflight missions. Compared to the highly toxic or hazardous nature of industry propellants, hybrid rocket propellants are significantly safer for both humans and the environment [1]. Because hybrid systems only require a single fluid flow path, they are of similar complexity to monopropellant systems; but with significantly higher performance. Applications for hybrid rocket motors include, but are not limited to, satellite station keeping and de-orbit, sounding rockets [2,3], orbital insertion for SmallSats [4,5], upper stages for Nano-launchers [6], and surface launch systems for Mars and Lunar Sample return missions [7].

While a hybrid rocket stage will likely have a higher dry mass as compared to a solid-propelled stage, the capability for throttle [8,9], on-demand ignition, shut-down, and re-ignition [10,11,12,13] allow the potential for in-flight propulsive trajectory adjustments. Launch vehicles propelled by solid stages cannot throttle or restart and must often rely on

"loiter"[14] to accomplish in-flight trajectory adjustments, which has a significant associated mass penalty. In fact, because of the above-described capabilities, hybrid rocket systems offer the potential to couple propulsion with the vehicle trajectory. When this linkage is properly optimized, several studies [15] have shown that hybrids have the potential to significantly out-perform solid propellant rocket systems.

However, the operational principles of hybrid motors are significantly different than those of solid rockets. For solid propellant systems, the oxidizer-to-fuel ratio is set by the propellant chemistry formulation to run slightly fuel-rich. Typically, a slightly fuel-rich operation gives the optimal characteristic velocity c^* performance, and also eliminates highly-reactive and potentially erosive unburned oxygen radicals in the exhaust plume. This O/F remains constant during the life cycle of a solid motor. Hybrid rockets, however, undergo a continual shift in *O/F* ratio as the fuel port burns, increases in diameter, and increasingly exposes more surface area. This O/F shift is endemic for hybrid rocket propulsion. Even for a constant oxidizer massflow rate, the O/F shift results in variable thrust, flame temperature, specific impulse over time, and a decrease in combustion efficiency. A large majority of hybrid system experience a continual shift in *O/F* with the motor gradually burning leaner with time [16]. This behavior exposes hybrid rockets to a greater concentration of oxygen-rich exhaust by products than is experienced by solid rockets, and can lead to erosion of motor exhaust-path flow components.

Thus, the O/F shift introduces considerable uncertainty into the total impulse time-distribution of the motor burn. Multiple researchers including Casalino and Pastrone (2015)[6], Casalino and Pastrone (2016)[17], Casalino et al (2019)[18], and Betts[14] have investigated approaches for trajectory optimization using hybrid propulsion. A primary conclusion is that model uncertainties can result in significant performance deviations from the nominal prediction. In some cases, uncertainties resulted in deviations so large that the expected mission objectives could be not achieved.

For typical hybrid rocket propellants, there exists only a narrow O/F range over which optimal performance is achieved. Figure 1 shows this effect where the characteristic velocity is plotted as a function of O/F ratio assuming gaseous oxygen (GOX) and Acrylonitrile Butadiene Styrene (ABS) as propellants. The plotted values were calculated using the industry-standard NASA Chemical Equilibrium with Applications (CEA) tool [19]. These calculations assume 100% combustion efficiency η^*, and were performed with increasing oxidizer-to-fuel *O/F* ratios and combustion pressure levels across a range of combustion (chamber) pressures P_0, varying 345 kPa (50 psia) to 5516 kPa (800 psia) in 170 kPa (25 psi) increments. Increasing values c^* are associated with increasing combustion pressures. The stoichiometric O/F ratio, approximately 2.29, is also plotted as the vertical dashed line. The red rectangle plotted in Figure 1 shows that the optimal O/F operating range for the propellants is very narrow, and moderately fuel-rich.

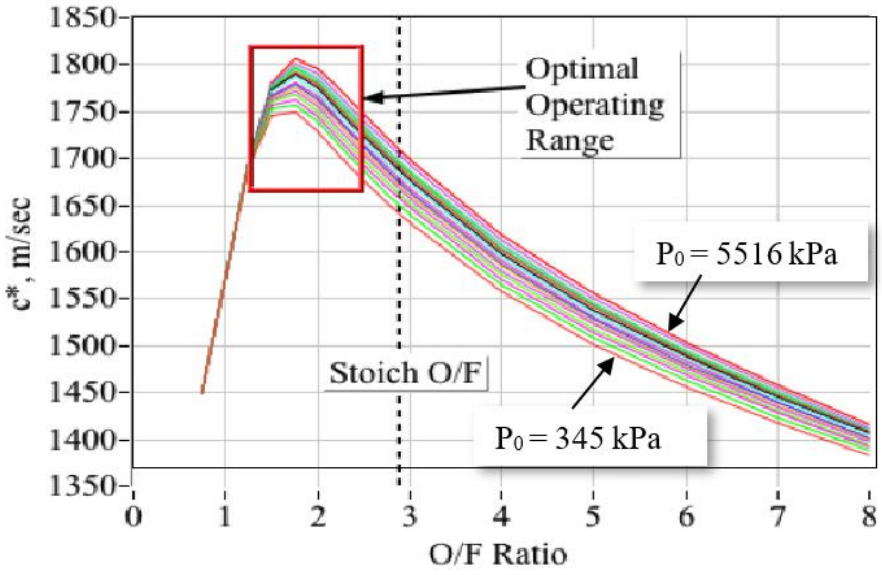

Figure 1: CEA-Derived Flame Characteristic Velocity for GOX/ABS Combustion

Even for a hybrid system that is initially optimized to give maximum performance at the beginning of the burn lifetime, the O/F shift, either positive or negative, will drive the motor away from optimal conditions, resulting in sub-optimal performance during the majority of the rocket's burn lifetime [20].

Development of a compensation method that eliminates the O/F Shift, irrespective of the shift magnitude or direction, would be of considerable advantage. Such a methodology has the potential to eliminate the-above discussed issues, thereby removing a significant obstacle to hybrid motor adoption in a wide range of spaceflight applications. This thesis describes the development, testing, and verification of an O/F compensating methodology for hybrid rocket motors.

1.2 Hybrid Combustion Modeling

1.2.1 Combustion and Fuel Pyrolysis in Hybrid Rockets

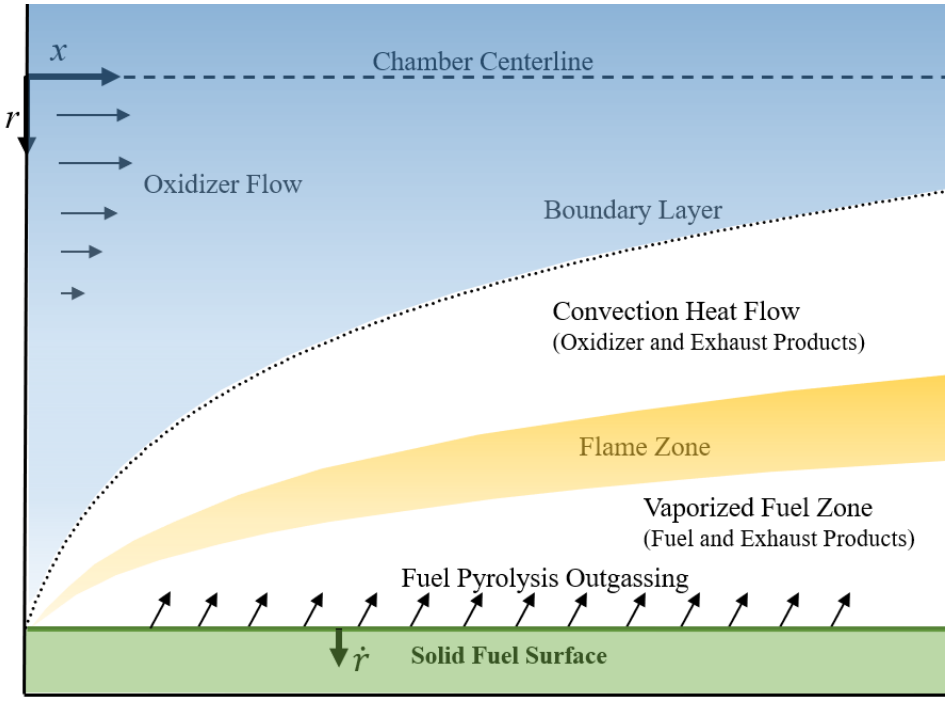

Figure 2: Hybrid Motor Combustion Process

As illustrated by Figure 2, Early studies by Marxman and Gilbert [21] (1963) and Marxman [22] (1964) demonstrated that combustion processes for hybrid rockets, and the associated fuel pyrolysis rates, are mostly driven by viscous heat transfer within the boundary layer. Thus, fuel regression rate is strongly correlated with the massflux through the combustion chamber fuel port. Marxman and Gilbert developed models incorporating a “blowing coefficient”, which attempts to quantify the effects of vaporizing fuel “blowing” the flame zone away from the surface of the fuel grain, thereby reducing convective heat transfer and skin friction at the combustion chamber walls [23]. Marxman and Gilbert developed a simplified model to predict the radial regression rate of fuel as follows [21]:

$$\dot{r} = \frac{.036}{\rho_f}\left(\frac{\mu_\infty}{x}\right)^{0.2} \frac{G^{0.8}B^{0.23}}{Pr^{0.7}} \quad (1)$$

Where regression rate $\dot{r}$, is defined in terms of fuel density ρ_f, dynamic viscosity μ_∞, distance from injector *x*, total massflux G, and Prandtl number Pr.

In Eq. (1), *B* is the blowing coefficient. Marxman and Gilbert's concept of "blowing" has served as a basis for most attempts to model hybrid rocket behavior, but correlation with experimental data shows that the Eq. (1) model requires correction to represent real behavior. Marxman and Gilbert also posed a length-dependent "Saint-Roberts" type of power-law model of the form,

$$\dot{r} = a \cdot G_{ox}^{n} \cdot L^{m} \quad (2)$$

where *L* longitudinal distance down the fuel port axis, $\dot{r}$ is the longitudinal mean of the fuel regression rate, G_{ox} is the oxidizer massflux down the fuel port, and $\{a, n, m\}$ are empirically-determined constants. This model offers greater flexibility for hybrid motors, as it can be anchored to experimental data from real motors.

This flexibility is required because, in reality, the effects of fuel vaporization on hybrid combustion vary between fuel types and overall rocket size. For example, the 1963 model assumes that diffusion forces from vaporizing fuel dominate combustion dynamics, but experimental research has shown that low-massflux motors are heavily influenced by radiation heat transfer, and combustion dynamics in high-massflux systems are dominated by Gas-phase kinetic forces (Figure 3).

Mass Flux Level	Low	Medium	High
Description	Radiative heat transfer dominates due to optical transmissivity of propellant particles	Convective diffusion dominates as well as fully turbulent heat and mass transfer	Gas-phase kinetics on chemical reactions become more apparent

Figure 3: Mass Flux Relationship to Dominant Combustion Influences [24]

The initial studies performed by references [21] and [22] predicted values for $n \sim 0.8$, *and* $m \sim 0.2$ for the parameters of Eq. (2). The burn parameters as predicted by Marxman and Gilbert agree well for combustion of nitrous oxide (N_2O) and hydroxyl-terminated poly butadiene(*HTPB)* as propellants; but, as shown by Zilliac and Karabeyoglu [25], these parameters do not agree as well for other combinations of propellants, Although the results of many regression rate tests have proven that the power-law form of Marxman's regression rate law (Eq. (2)) is valid for non-erosive burning, to date there exists no comprehensive, first-principal theory that can be used to reliably predict this quantity over a range of propellants and motor sizes.

1.2.2 Modeling the Hybrid Motor O/F Shift

Ziliac and Karabeyoglu go on further to describe the previously discussed O/F shift process in terms of the Marxman burn parameters. They model the hybrid rocket fuel as a simple cylindrical port with oxidizer injected axially from the up-stream end of the motor, burning the fuel grain radially outward. As the fuel burns away, both the combustion chamber volume and the surface area of exposed fuel increase.

Assuming a fuel-regression rate of Eq. (2), the hybrid O/F shift is described by Eq. (3) where $\dot{m}$ is massflow rate and D_{port} is the fuel port diameter.

$$O/F = \frac{\dot{m}_{ox}}{m_{fuel}} = \frac{\dot{m}_{ox}}{\rho_{fuel}\cdot\left(A_{burn}\right)\cdot\dot{r}} = \frac{\dot{m}_{ox}}{\rho_{fuel}\cdot\left(\pi\cdot D_{port}\cdot L\right)\cdot\dot{r}} =$$

$$\frac{\dot{m}_{ox}}{\rho_{fuel}\cdot\left(\pi\cdot D_{port}\cdot L\right)\cdot\left(a\cdot G_{ox}^{n}\cdot L^{m}\right)} = \frac{\dot{m}_{ox}}{\rho_{fuel}\cdot\left(\pi\cdot D_{port}\cdot L\right)\cdot a\left(\frac{\dot{m}_{ox}}{\frac{\pi}{4}\cdot D_{port}^{2}}\right)^{n}\cdot L^{m}} . \quad (3)$$

Simplifying Eq. (3),

$$O/F = \left(\frac{1}{4^{n}\cdot\pi^{1-n}}\right)\cdot\left(\frac{\dot{m}_{ox}{}^{1-n}}{a\cdot\rho_{fuel}}\right)\cdot\left(\frac{D^{2n-1}}{L^{m+1}}\right) . \quad (4)$$

Evaluating the time-derivative of Eq. (4),

$$\frac{\partial\left(O/F_{(t)}\right)}{\partial t} = \left(\frac{1}{4^{n}\cdot\pi^{1-n}}\right)\cdot\left(\frac{\dot{m}_{ox}{}^{1-n}}{a\cdot\rho_{fuel}\cdot L^{m+1}}\right)\cdot\frac{\partial\left(D^{2n-1}\right)}{\partial t} =$$

$$\left(\frac{1}{4^{n}\cdot\pi^{1-n}}\right)\cdot\left(\frac{\dot{m}_{ox}{}^{1-n}}{a\cdot\rho_{fuel}\cdot L^{m+1}}\right)\cdot\left(\left(2n-1\right)\cdot D^{2n-2}\cdot 2\cdot\dot{r}\right) . \quad (5)$$

Substituting Eq. (5), $\dot{r} = a\cdot G_{ox}^{n}\cdot L^{m}$, and Eq. (A1.3) $G_{ox} = \dot{m}_{ox}\Big/\frac{\pi}{4}D^{2}$, and simplifying,

$$\frac{\partial\left(O/F_{(t)}\right)}{\partial t} = \left(\frac{2\cdot\left(2n-1\right)}{4^{n}\cdot\pi^{1-n}}\right)\cdot\left(\frac{\dot{m}_{ox}{}^{1-n}}{a\cdot\rho_{fuel}\cdot L^{m+1}}\right)\cdot D^{2(n-1)}\cdot a\cdot\left(\frac{\dot{m}_{ox}}{\frac{\pi}{4}D^{2}}\right)^{n}\cdot L =$$

$$\left(\frac{2n-1}{2}\right)\cdot\left(\frac{\dot{m}_{ox}}{\rho_{fuel}\cdot L\cdot\frac{\pi\cdot D^{2}}{4}}\right) = \left(\frac{2n-1}{2}\right)\cdot\left(\frac{\dot{m}_{ox}}{\rho_{fuel}\cdot L\cdot V_{port}}\right) \quad (6)$$

From Eq. (6), it is observed that as port diameter grows during the fuel burn; for a burn exponent with ***n > 1/2***, the O/F ratio experiences a positive shift and the motor burns increasingly *leaner with time*. For a burn exponent exactly equal to 1/2, the burn is neutral and the motor experiences *no O/F shift* with time. Finally, for burn exponent ***n < 1/2***, the motor burns increasingly *fuel rich with time*, and the O/F shift is negative. As

described previously, O/F shift originates from a decreasing oxidizer massflux over time, traded-off against an increasing fuel burn area. This behavior has a major influence on the observed motor burn profiles. Assuming a constant oxidizer massflow rate, a positive O/F shift motor will generally see a decrease in thrust as the motor burns, and a negative O/F motor will experience an increase in thrust with time.

Figure 4 illustrates this effect using experimentally-derived data collected for USU's 75-mm ABS/GOX motor. Plotted at (a) thrust, (b) massflow, (c) O/F ratio and (d) specific impulse. Note from Figure 2(b) that even though the oxidizer massflow rate is nearly constant and even drops slightly near the end of the burn; due to the negative O/F shift, the thrust and total massflow continuously rise during the course of the burn.

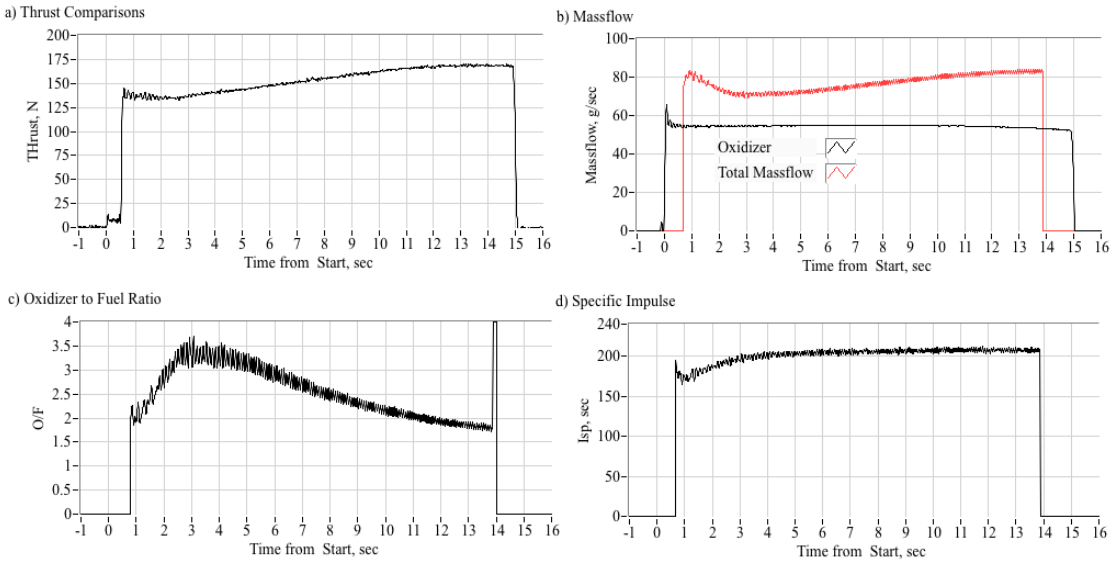

Figure 4: Effect of O/f Shift on Hybrid Motor Thrust and Specific Impulse Profiles

1.2.3 Controlling the O/F Shift Hybrid Rockets

In order to manipulate O/F ratio and maintain throttle control, it is necessary to alter the regression rate independently of oxidizer mass flow. A faster regression rate will result in more fuel entering the plume and a lower O/F. This project attempts to control regression rate, and by extension O/F, by varying vorticity in the combustion chamber. Increased vortex strength pushes the flame zone closer to the fuel grain and results in greater skin friction between combustion gasses and the fuel solid fuel surface (Figure 2). The regression rate then increases. The Japan Aerospace Exploration Agency (JAXA) has demonstrated increased regression rates and O/F manipulation in hybrid rockets using swirl oxidizer injection [26]. With a solid theoretical foundation and demonstrated effectiveness, this project anticipated vortex manipulation would be an effective tool for O/F control.

Because vortex manipulation attempts to control the total O/F ratio by manipulating both the oxidizer and fuel massflow rates, the regression rate model of Marxman and Gilbert, Eq. (2), is modified to allow the total massflow rate to drive the fuel pyrolysis,

$$\dot{r} = \frac{a \cdot G_{total}^{n}}{L^{m}} \tag{7}$$

For simplicity, since the data to be presented in this report only consider one motor length, the model of Eq. (7) is further simplified to be

$$\dot{r} = a \cdot G_{total}^{n} \tag{8}$$

Previous attempts have been made to model the effects of vorticity. JAXA has developed a swirl motor similar to the USU design. Jérôme Messineo and Toru Shimada utilized Eq. (9) in their development of a feedback control law [26]:

$$\dot{r}(t) = 4^n \pi^{-n} a \left(1 + S_g^2 \frac{\dot{m}_{OxT}^4(t)}{\left(\dot{m}_{OxA}(t) + \dot{m}_{OxT}(t)\right)^4}\right)^m \left(\frac{\dot{m}_{OxA}(t) + \dot{m}_{OxT}(t)}{d_{port}^2(t)}\right)^n \tag{9}$$

Where S_g is "swirl number", $\dot{m}_{OxA}$ is axial oxidizer mass flux, and $\dot{m}_{OxT}$ is tangential oxidizer mass flux (the JAXA swirl motor injects oxidizer tangentially to create vortex flow in the chamber). This model is analogous to the "generic model" in that the "swirl number" is a constant that can be tuned by experimental data to match each motor's unique geometry.

By contrast, Whitmore and Walker et. al. (2015) and (2017) [27] developed a model which attempts to predict the effects of skin friction, Eq. (10), and blowing suppression, Eq. (5) [6].

$$A_{Cf} = 1 + \frac{0.0075}{C_{fstraight}} \sqrt{\frac{2r_L(t)}{2R_{ceff}}} \tag{10}$$

$$A_\beta = \left[1 + 2(2\pi N)^2 \left(\frac{O}{F}\right)^2 \frac{M_{w_{wall}}}{M_{w_{ox}}} \left(\frac{2r_{helix}}{2r_{L(t)}}\right)\right]^{0.77} \tag{11}$$

These values are incorporated into the generic model in Eq. (12).

$$\dot{r} = A_{Cf} A_\beta a (G_{total})^n \tag{12}$$

This model, however, attempts to quantify vorticity effects in a motor with a traditional injector and helical port. Despite this discrepancy, the model provides a useful approach to predicting the behavior of the vortex injection design.

This review of past approaches to hybrid rocket modeling provides a basis for USU's prediction and analysis, namely the development of a numerical engineering model. This model is described in 1.2.4.

1.2.4 Numerical Model Predictions

The numerical modeling approaches described in Section 1.2.2 were each investigated and implemented to determine the validity of O/F control via vortex strength manipulation. By adopting the "generic model" for hybrid rocket performance, the numerical predictions more closely approximate experimental results. The generic model is compared to the experimental data of Figure 4 in Figure 5 and Figure 6.

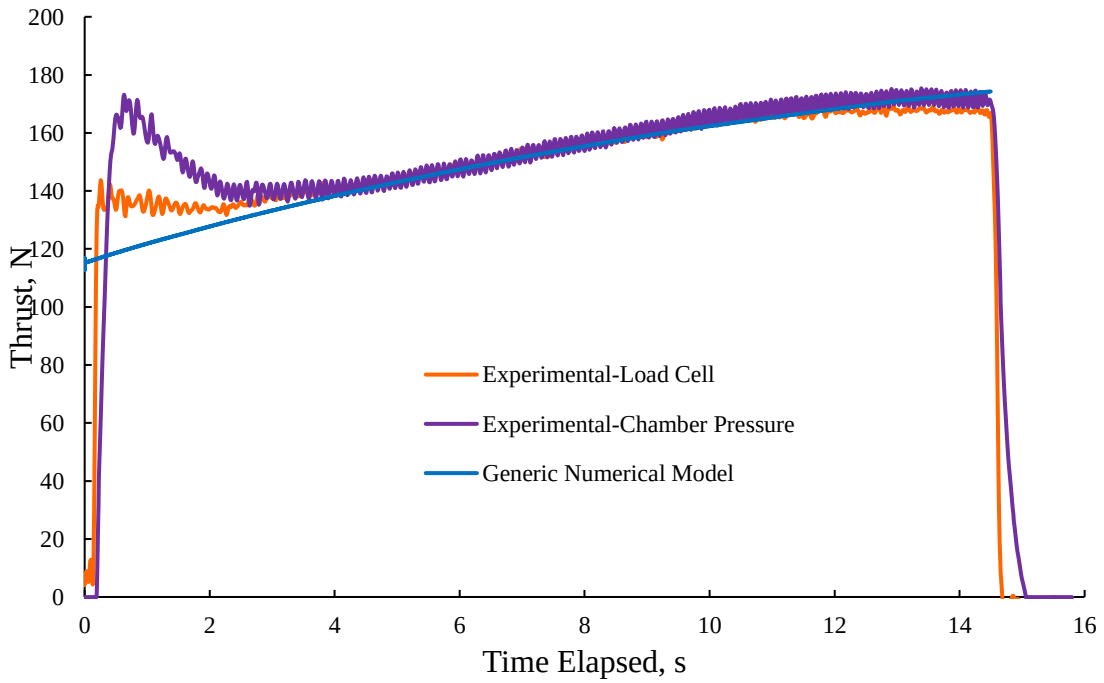

Figure 5: Generic Model Predicted Thrust vs Experimental Data

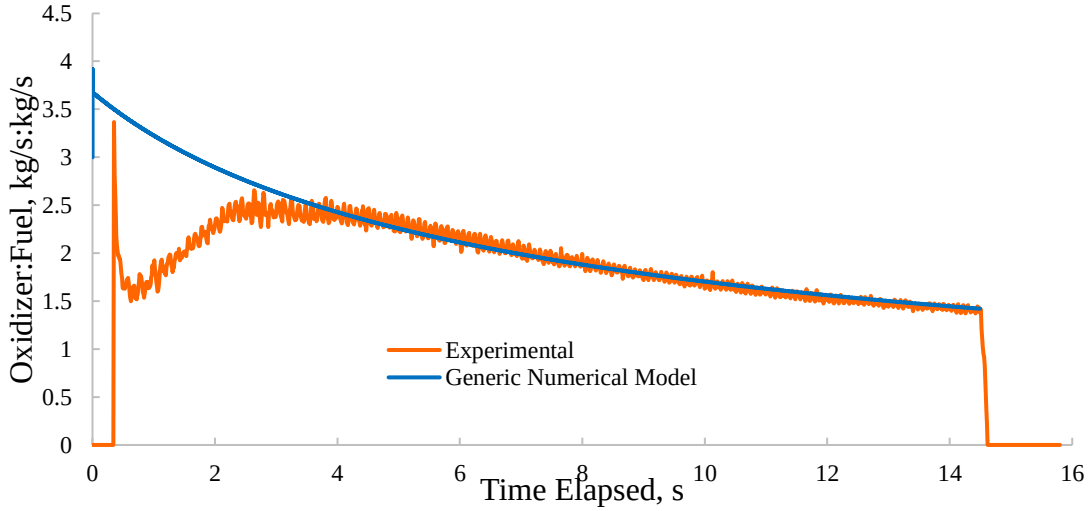

Figure 6: Generic Model Predicted O/F vs Experimental Data

Values for the burn coefficient and burn exponent are matched as closely as possible to experimental data. USU's experimental data for the ABS-GOX motor matches Eq. (13). The regression rate is measured in meters per second.

$$\dot{r} = 4.9 \cdot 10^{-5} (G_{total})^{0.14} \tag{13}$$

Compare the values of an ABS-GOX motor to traditional hybrid propellant combinations:

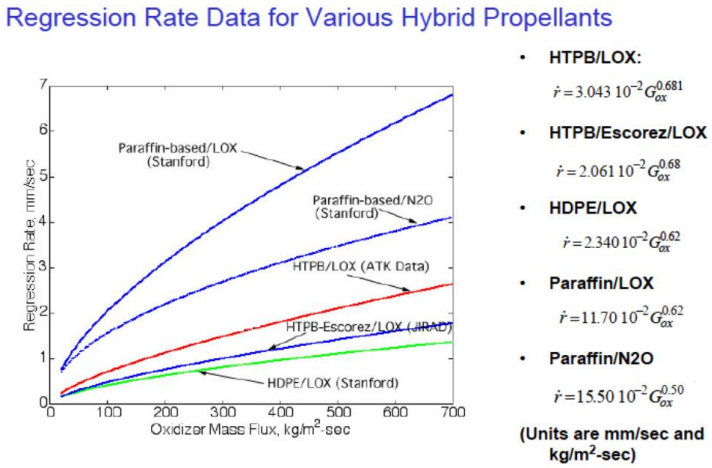

Figure 7: Regression Rate Data for Various Hybrid Propellants [28]

The model is then modified to account for the effects of vorticity. Eq. (14) is an extension of the generic hybrid regression model incorporating the swirl element of Eq (9). Re-written using the same terms as the generic numerical model, the swirl model becomes Eq. (8).

$$\dot{r} = a(G_{total})^n\left(1 + S_g(V_{ratio})^4\right)^m \tag{14}$$

Where V_{ratio} is the ratio of oxidizer injected forward of the screw to oxidizer injected axially. S_g is the "swirl number", a constant dependent on injector geometry and m is the secondary burn exponent. S_g and m, similar to the constants of the generic equation, are matched with data experimentally. Because no experimental data for USU's swirl motor was available during predictive modeling, the numerical model is populated with values used by Jérôme Messineo and Toru Shimada for the JAXA motor, such that $S_g = 50$ and $m = 0.1392$ [26]. Note that these constants are expected to vary, similar to the regression rate data in Figure 7, dependent on the fuel-oxidizer combination. The model is matched to the experimental vortex motor data in the results section of this document.

The vortex numerical model uses a Runge-Kutta 4 integrator to propagate the state equations of the motor. Chemical reaction properties in the combustion chamber are calculated with pre-generated tables using NASA's CEA software [19]. Results generated in this document used a 0.0005s timestep. USU's motor in constructed with an initial port diameter of 0.5in, a nozzle throat diameter of 0.55in, and a total length of 12.4in. Gaseous oxygen is injected at 350psig through a 0.1in diameter injector. Pressure feedback effects on oxidizer massflow are captured in the numerical model.

Figure 8 displays the predicted sensitivity of motor performance to Vortex Ratio, simulating constant-throttle burns at the same oxidizer massflow levels as the generic model correlation burn shown in Figure 5 and Figure 6.

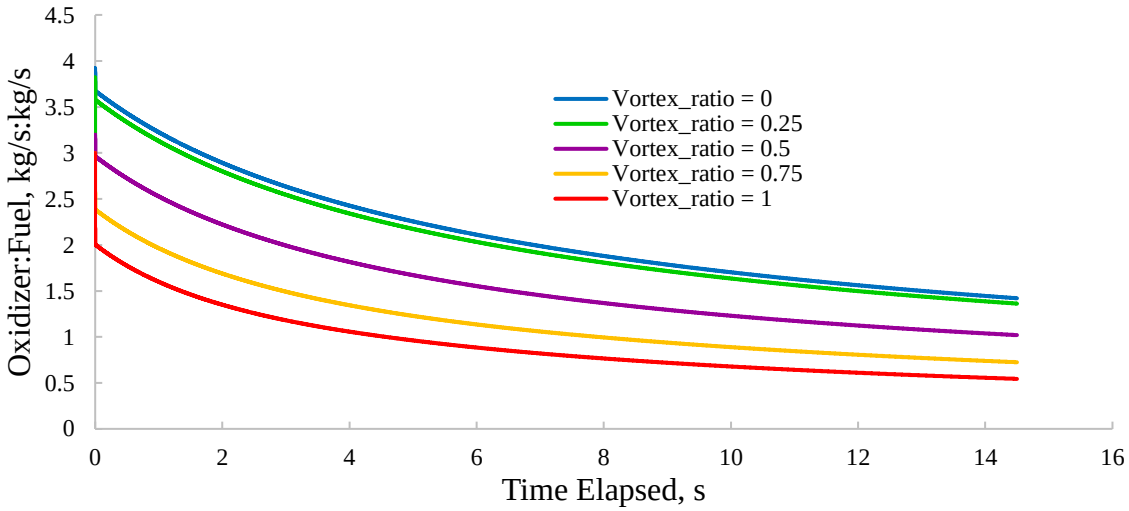

Figure 8: Numerical Model O/F Profiles at Varying Vortex Ratios, Sg=50, m=0.1392

Vortex ratio has a strong effect on all monitored performance parameters, but has the greatest proportional effect on O/F values. This is the intended response to varying vorticity, and O/F decreases in response to increasing vorticity as expected. Note that specific impulse is primarily dependent on optimal combustion conditions, such that optimal Isp occurs only at one O/F condition (O/F ≈ 1.5, see Figure 1).

The desired application of vorticity control is the ability to dictate O/F in the motor at any point during a burn, compensating for natural shift. If O/F can be maintained at optimal conditions, efficiency at all points in time during a burn will increase. A simple proportional control loop in the numerical model is used to vary vortex strength in response to O/F shift. The target O/F value is 1.5. Figure 9 through Figure 12 display the results of the control loop's introduction.

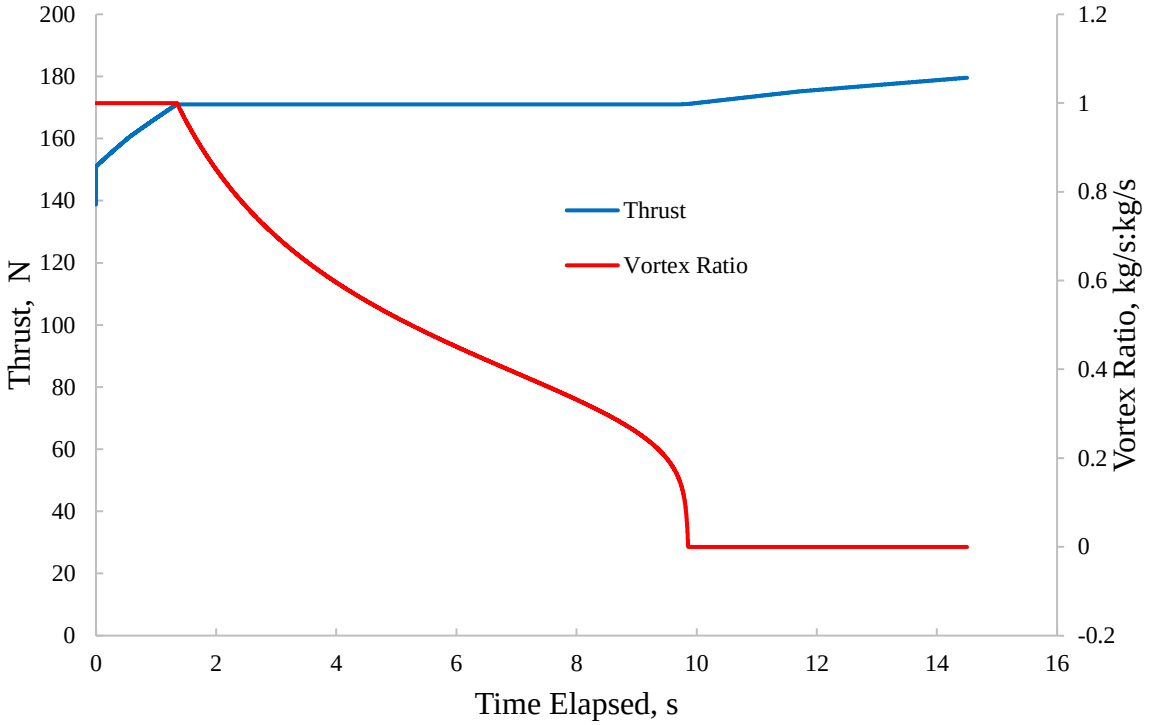

Figure 9: Thrust Profile with Vortex O/F Compensation

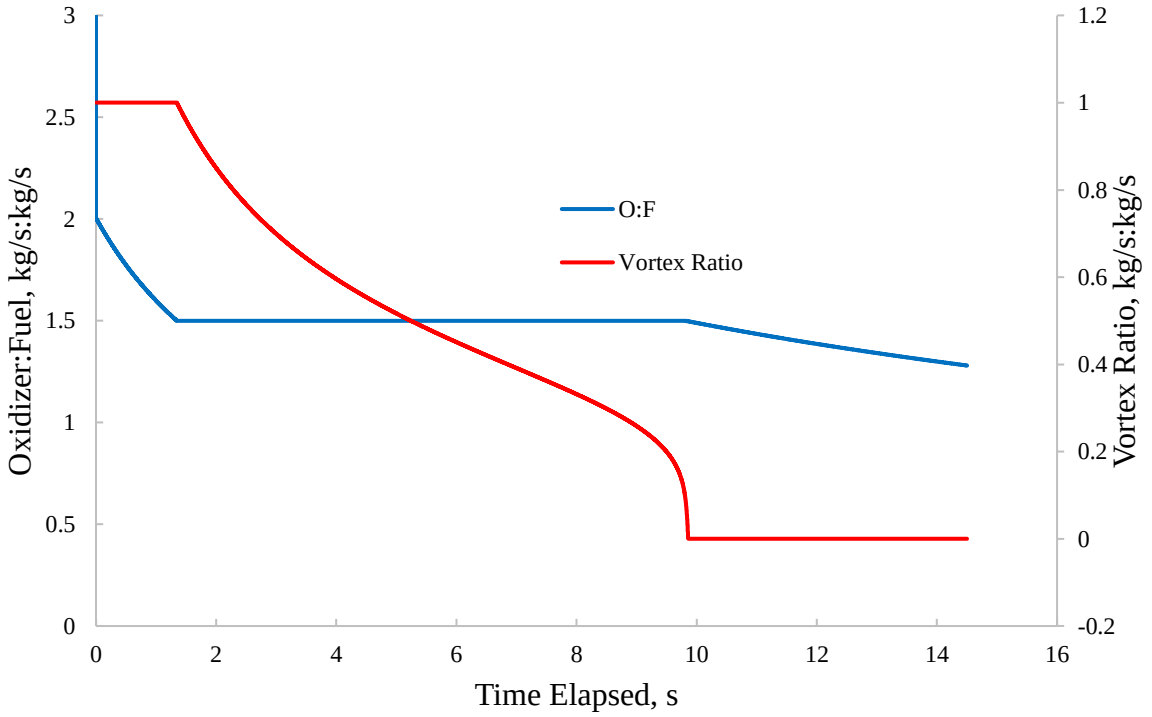

Figure 10: O/F Profile with Vortex O/F Compensation

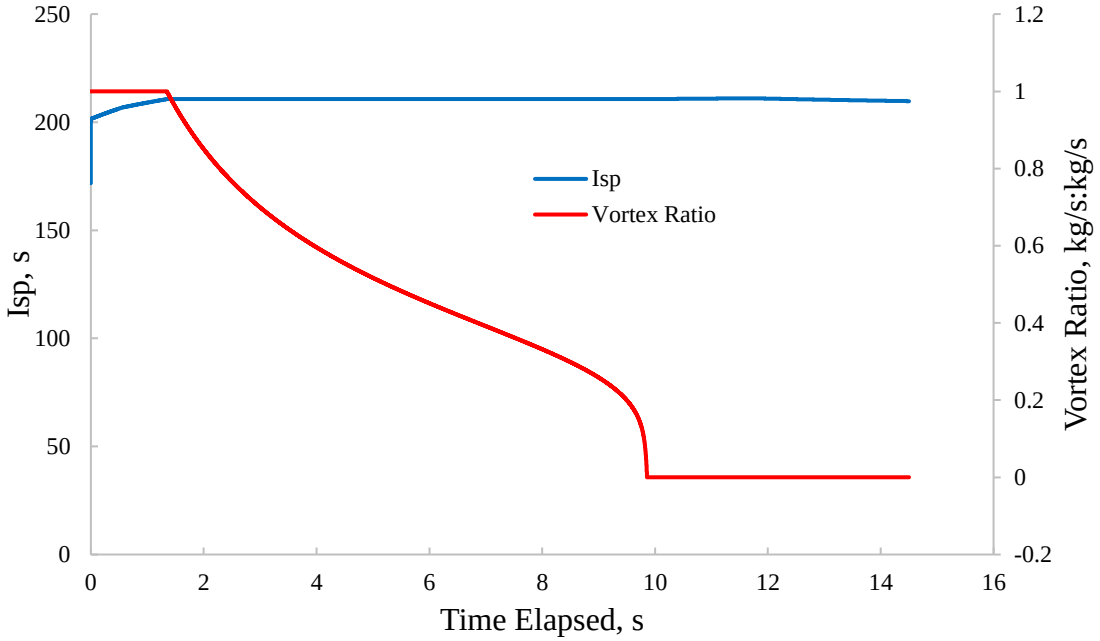

Figure 11: Specific Impulse Profile with Vortex O/F Compensation

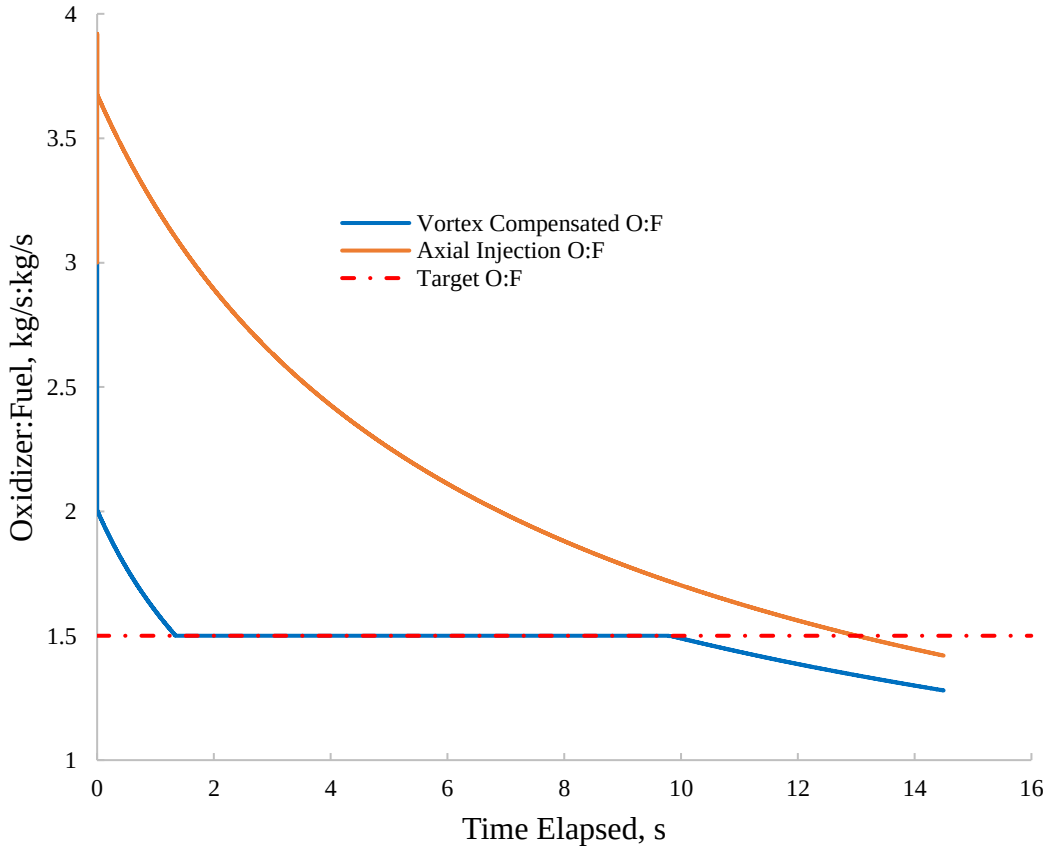

Figure 12: Numerically Modeled O/F Compensating Burn vs Axial-Injection Burn

In response to vorticity control, the model successfully compensates for natural O/F shift and significantly increases the efficiency of the motor from an average Isp of 197.7 to 209.8s, an improvement of over 6%. Note that this model underestimates specific impulse when compared to experimental data. Thrust is also more consistent, providing a steady burn profile.

The vortex injector has a limited ability to control motor behavior. Combustion chamber geometry constantly changes in a hybrid motor. As a result, the vortex ratio reaches its maximum bound at the beginning of the burn and the minimum towards the end. Vorticity control has an overall positive effect on the motor, but is unable to maintain optimal O/F during the entire burn. However, the swirl constants used in these predictions are not experimentally verified. The results section of this document describes the experimentally-measured effect of vorticity on O/F ratio. Despite this uncertainty in the numerical model, the general performance trend results validate the vortex motor design's feasibility for controlling O/F.

1.3 Proposed Solution

This research will implement the described theoretical background with the aim of demonstrating commanded O/F manipulation by varying vorticity in the combustion chamber. Minimal complexity will help isolate motor input and output metrics in order to best identify and understand motor behavior. Additional plumbing, valves, moving parts, and modifications to the existing motor and test infrastructure should be reduced as much as possible. Vorticity control, therefore, will be achieved by replacing USU's legacy injector with a newly-designed vortex control injector.

The injector will be placed in-line with the legacy test setup, in-between the test infrastructure and oxidizer supply and the combustion chamber. This approach allows flexibility in configuration and commandability, and results in a solution that is applicable to other motor designs and configurations with minimal modification.

1.4 Thesis Statement

The objective of this thesis is to investigate and quantify the effects of injection-controlled vorticity in an ABS-GOX hybrid rocket motor. A variable vorticity injector is designed and tested. The resulting experimental data is used to develop a final O/F shift compensating 98mm hybrid rocket motor.

1.5 Overview

The remainder of this document will detail the objectives and approach of the thesis project. The methodology section describes the project's approach to hardware engineering, software development, the experimental test campaign, and experimental data analysis. The results section details the events of the test campaign and analyzed data. The thesis concludes by evaluating the success of the project and identifying future progress to build off of the results.

CHAPTER 2

METHODOLOGY

2.1 Introduction

This section describes the methodology used to develop the O/F compensating motor. Producing a functional motor required an iterative engineering process to correct design flaws and improve performance. The section includes the initial design, the resulting motor failure, and corrective design changes. Command software development and data analysis methods are explained and documented.

2.1.1 Hardware Engineering

The injection system allows for both axial and swirl (vortex) injection, with the ability to remotely switch between the two during a burn. The injector is intended to be minimally complex and can survive multiple burns and motor assemblies. The injector also allows for combustion chamber pressure monitoring, electrical ignition, and fiberoptic spectroscopy cable feedthrough. Previous swirl motor designs have utilized tangential injection, inserting the swirl through the side casing [26]. Among other undesirable effects, this compromises the pressure vessel, requiring a casing redesign. This project modified USU's existing 98mm motor. Therefore, this injector design confines the entire injection system to the endcap. Compare the legacy USU motor design to the vortex motor (Figure 13 and Figure 14).

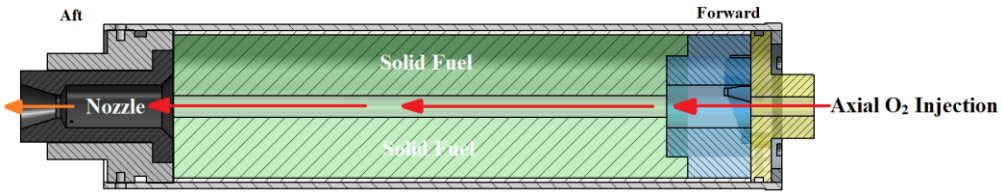

Figure 13: Legacy USU Hybrid Motor Cross-Section (Baseline)

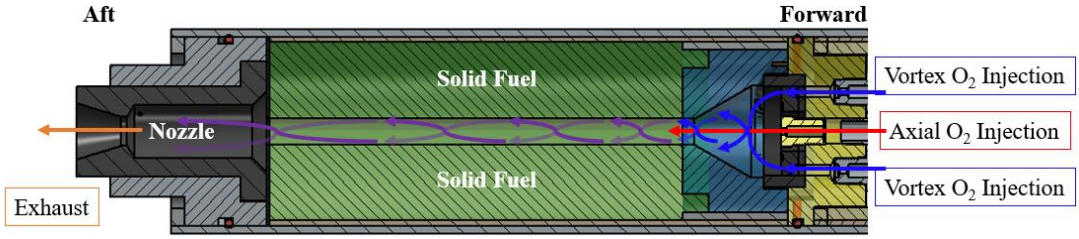

Figure 14: Vortex Injection Hybrid Motor Cross-Section

Various critical design features contribute to the vortex motor's functionality:

- Direct oxidizer impingement on the fuel grain can cause undesirable asymmetric erosion, shortening the life of the motor. Therefore, the injector design attempts to distribute oxidizer pressure exiting the impeller evenly around the circumference of the port. This is accomplished via a "dispersion ring" (Figure 15 and Figure 16)
- The addition of the impeller requires a larger initial volume in the forward-end port. This results in decreased material and thinner walls in the vortex spark cap relative to the traditional axial spark cap. A stainless steel guard ring was implemented as burn-through prevention.
- Oxidizer-rich combustion in the forward end produces high temperatures and erodes components. The impeller and dispersion ring extend minimally into the chamber and are comprised of machined graphite; a relatively low-cost material that can withstand forward-end conditions.

- The diameter of the impeller is maximized and the pitch minimized in within the design constraints.
- The existing 98mm motor was modified to accommodate the new injector. In order to increase the baseline O/F, the fuel grain length was shortened. The spark cap was also modified to interface with the injector.

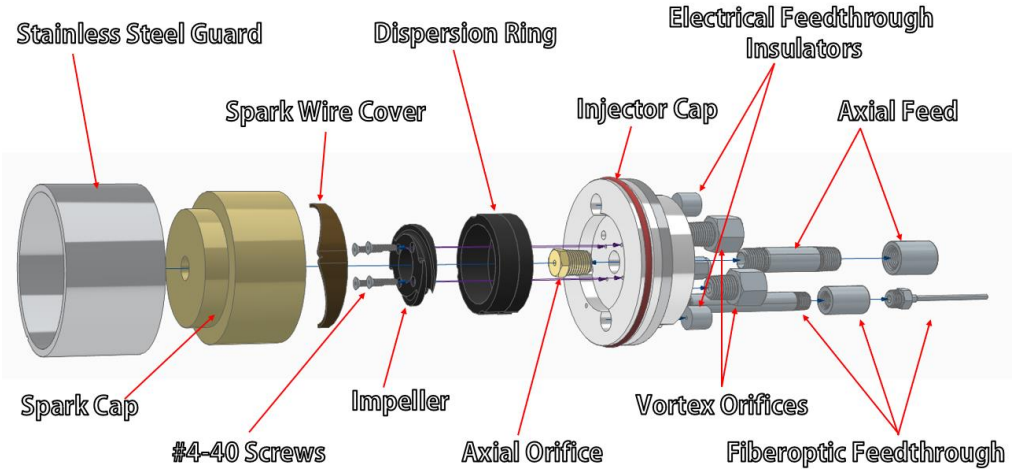

Figure 15: Injector Re-Design Exploded View

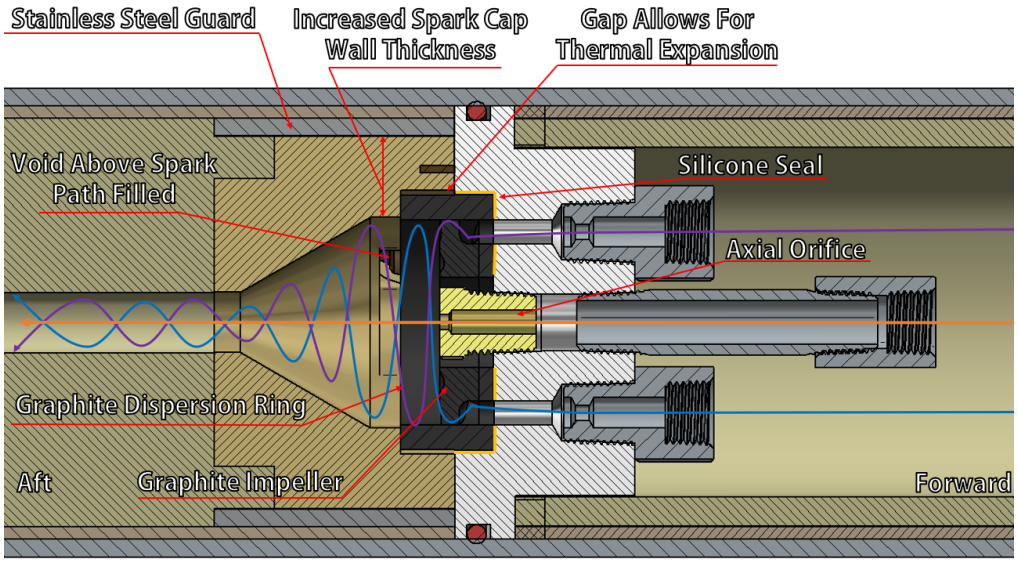

Figure 16: Injector Re-Designed Features Cross-Section

Vortex strength control is achieved through pulse width modulation. In order to limit the mass and complexity of the system, one solenoid controls each oxidizer flow path to the injector. Only a single solenoid is allowed open at any point in time (implemented via software to maintain flexibility). A pulse-width modulation control actuator allows mean vortex strength control. A time interval is set such that the percentage time that the swirl injection solenoid is open is directly proportional to the desired vortex strength. The injector solenoids are controlled through 24V DC to 120V AC electrical relays.

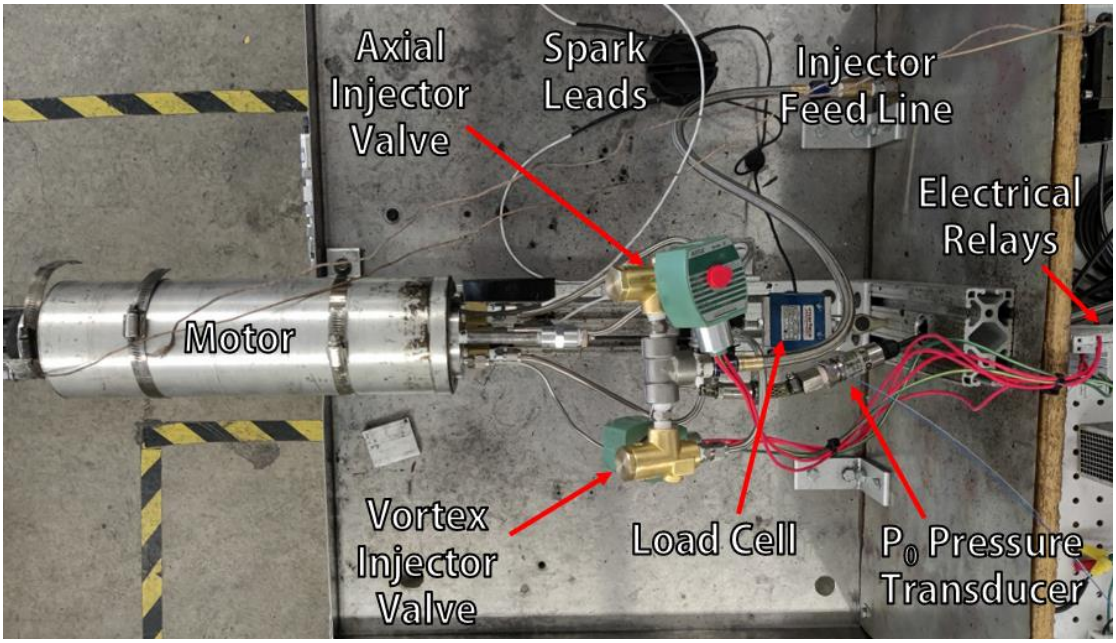

Figure 17: Motor Test Configuration

2.1.2 Injector Sizing

O/F shift compensation in a motor should ideally operate independently of throttle. This increases the mission profile flexibility of the motor. Because vortex strength is manipulated using pulse width modulation, the total thrust produced by axial injection should be approximately the same as thrust produced by vortex injection. Initial tests were performed with orifices sized such that oxidizer massflow would be identical through axial injection or vortex injection. Thrust produced with pure axial injection and thrust produced with pure vortex injection were measured, after which the vortex orifices were resized according to oxidizer massflow predictions where:

$$\dot{m}_{inj} = C_d P_0 A_{inj} \sqrt{\frac{\gamma}{R_g T_0}\left(\frac{2}{\gamma+1}\right)^{\frac{\gamma+1}{\gamma-1}}} \tag{15}$$

Injector discharge coefficients are calculated using ASME standard orifice fluid flow measurement calculations [32] [33]. For increased accuracy, Eq. (16) through (19) are iterated until converging on a final value C_d [34].

$$\rho_{ox} = \frac{P_0}{R_g T_0} \tag{16}$$

$$Re_D = \frac{4\dot{m}_{inj}}{\pi D \mu_{ox}} \tag{17}$$

$$C_v = \left(0.598 + 0.468\left(\left(\frac{d}{D}\right)^4 + 10\left(\frac{d}{D}\right)^{12}\right)\right)\sqrt{1-\left(\frac{d}{D}\right)^4} + \left(0.87 + 8.1\left(\frac{d}{D}\right)^4\right)\sqrt{\frac{1-\left(\frac{d}{D}\right)^4}{Re_D}} \tag{18}$$

$$C_d = \frac{C_v}{\sqrt{1-\left(\frac{d}{D}\right)^4}} \tag{19}$$

Using the above method establishes a relationship between injector orifice diameter and oxidizer massflow (Figure 18). Assuming oxidizer massflow is proportional to total massflow for vortex injection, orifices were resized such that total vortex massflow is approximately equal to total axial massflow at T<10s.

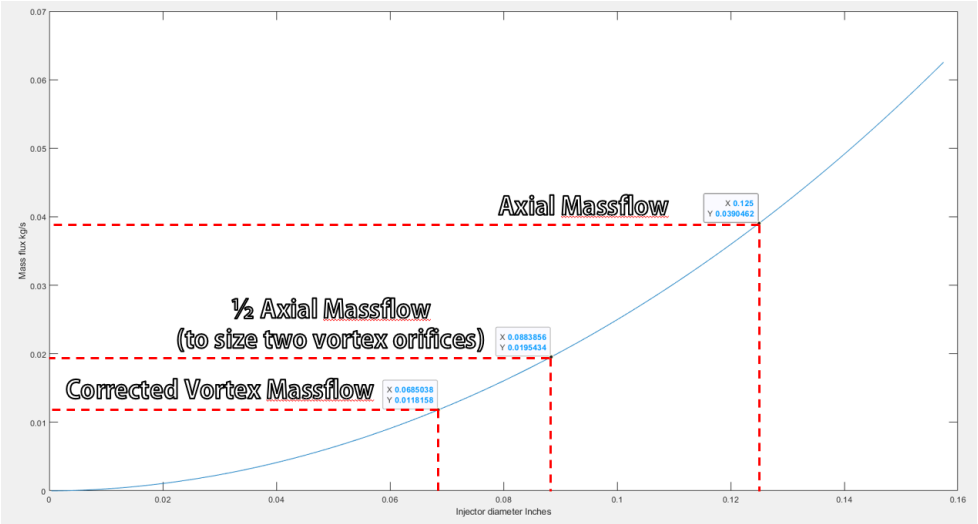

Figure 18: Massflow vs Injector Diameter (inches) at Standard Motor Test Conditions

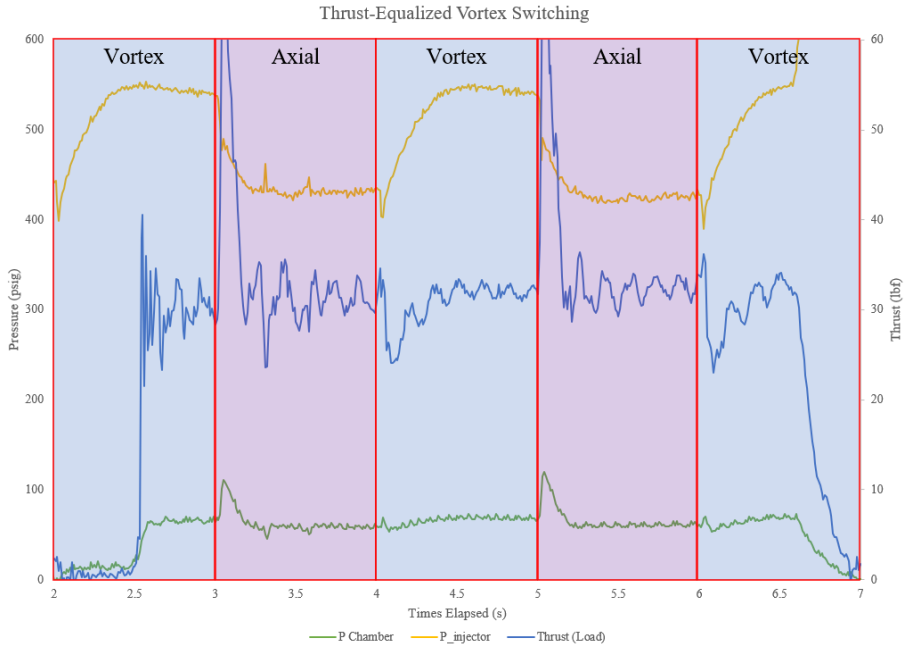

Figure 19: Thrust-Equalization Test Burn. F_{load}, P_{feed}, and P_0 vs Elapsed Time

This total massflow compensation was tested with a 50% vortex strength, 2s period burn, where load cell thrust measurement was considered analogous to total massflow. In the final configuration, which successfully equalized massflow at steady state (Figure 19), $\dot{m}_{ox\_vortex} = 0.61\dot{m}_{ox\_axial}$.

2.1.3 Test Software Development

Existing National Instruments LABVIEW software used to command the rocket cart and throttle was modified to include additional manual controls for vortex strength. Each electrical relay is commanded open or closed based on the time-dependent vortex strength setpoint and pulse width period.

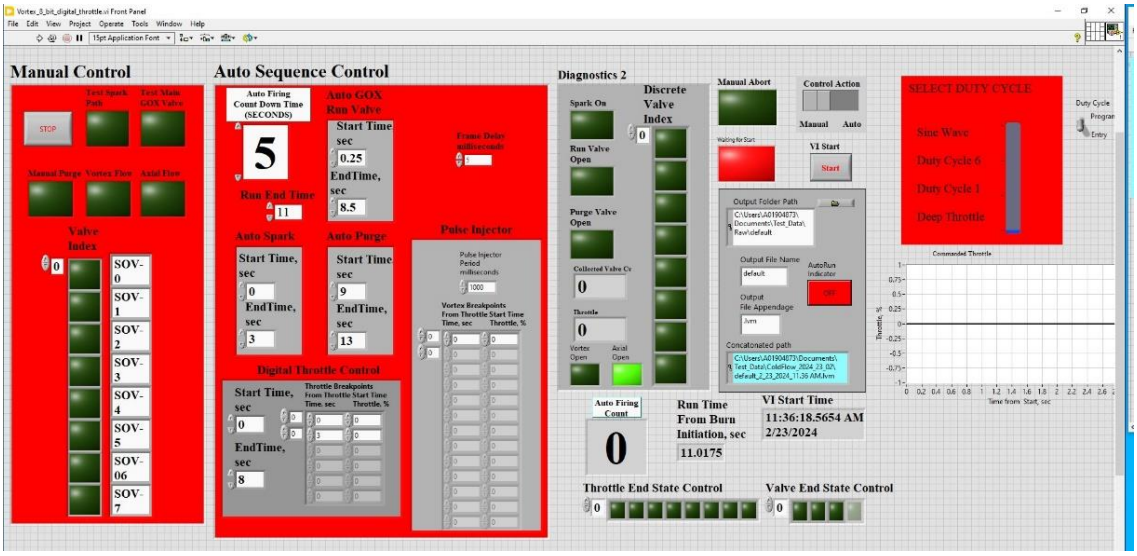

Figure 20: Test Control Software Panel, LABVIEW 2022

2.1.4 Data Collection

Data collection will be performed with existing USU hardware and software, building upon the Propulsion Research Laboratory's previous work developing non-invasive measurement techniques [35]. Hot fires were performed by Propulsion Lab personnel within USU's propulsion test cell, also known as the BLAST Lab. Performance data is run through a lowpass filter prior to analysis to filter out noise.

Table 1: Relevant Measurements Collected During Hot Fire Testing

Symbol	Measurement Description	Units	Instrument
F_{load}	Thrust	Lbf	Load Cell
P_{tank}	Ox Tank Pressure	Psig	Pressure Transducer
P_{feed}	Injector Feed Pressure	Psig	Pressure Transducer
P0	Chamber Pressure	Psig	Pressure Transducer
V	Igniter Voltage	Volts	Multimeter
I	Igniter Current	Amperes	Multimeter
P_{dig_in}	Throttle Valve Inlet Pressure	Psig	Pressure Transducer
P_{dig_out}	Throttle Valve Outlet Pressure	Psig	Pressure Transducer
T_{tank}	Ox Tank Temperature	°C	Thermocouple
T_{reg}	Regulator Temperature	°C	Thermocouple
T_{feed}	Injector Temperature	°C	Thermocouple
m_{tank}	Ox Tank Mass	g	Digital Scale
m_{fuel}	Fuel Grain Mass	g	Digital Scale
N/A	Combustion Chamber Spectra	Amplitude vs Wavelength	Spectrometers

Table 1 lists the measured parameters taken for each burn that are used to analyze motor performance. Pressure transducers are amplified strain gauges with a sample rate of 100hz, thermocouples are type-K sampled at approximates 2hz, and the load cell uses an unamplified 4-arm Wheatstone bridge. Because the uncompensated load cell is susceptible to temperature changes and many of the presented test data were obtained at frigid temperatures as low as -15 deg. C, this project will use load cell data only qualitatively. The low operating temperatures significantly affected the increased the load cell scale factors and bias readings, and these temperature effects on the load cell readings were not discovered until the completion of the data collection phase, and the sponsor schedule and budget constraints would not allow the test series to be re-performed using a compensated device.

Thus, the primary thrust measurement used for this project is derived using the chamber pressure, calculating the thrust using the 1-dimensional de Laval Flow equations, from Anderson [36] Chapt. 5, using the measured chamber pressure P_0, nozzle exit area A^*, and exhaust gas properties as inputs,

$$F_{P_0} = P_0 A^* \cdot \left(\sqrt{\frac{2}{\gamma - 1} \cdot \left(\frac{2}{\gamma + 1} \right)^{\frac{\gamma+1}{\gamma-1}} \left(1 - \frac{p_{exit}}{P_0} \right)^{\frac{\gamma-1}{\gamma}}} + \left(\frac{A_{exit}}{A^*} \right) \left(\frac{p_{exit} - p_\infty}{P_0} \right) \right) \tag{20}$$

In Eq. (20) A_{exit} is the nozzle exit area, p_{exit} is the nozzle exit plane static pressure, and p_∞ is the local operating ambient pressure level. This calculation assumes negligible nozzle erosion during the burn.

Igniter voltage and current measurements are only used to anchor the open loop command start time, T+0s. Fuel grain mass is taken before and after a burn, while all other measurements are taken in real time.

2.1.5 Analysis and Modeling

Evaluation of O/F compensation requires an accurate and reliable estimate of time-dependent O/F. Because USU is not currently equipped to directly measure motor O/F, the value must be derived from the data collected according to Table 1.

O/F ratio can be derived using chamber pressure, oxidizer massflow, compressible fluids equations, motor geometry, and combustion analysis of the relevant propellants. For the purposes of this project, the most critical compressible fluids equation is Eq. (21) [24].

$$\dot{m}_{total} = A_{throat} \frac{P_0}{\sqrt{T_0}} \sqrt{\frac{\gamma}{R_g} \left(\frac{2}{\gamma + 1}\right)^{\frac{\gamma+1}{\gamma-1}}} \tag{21}$$

$$O_F = \frac{\dot{m}_{ox}}{\dot{m}_{total} - \dot{m}_{ox}} \tag{22}$$

The chamber pressure using a temperature-compensated, amplified, pressure transducer that was not susceptible to the temperature effects as observed on the load cell readings. The relationship between chamber pressure, O/F, and the other exhaust gas properties T_0, $R_g = R_u/M_w$, and γ is estimated using NASA's CEA software [19]. CEA data is imported into analysis software as three 2D tables: Flame Temperature (T_0), Molecular Weight (M_w), and Specific Heat (γ). The analysis software uses a table lookup with P_0 and O/F as inputs.

Total massflow is estimated by computing Eq. (21) for a range of possible O/F. This produces a wide range of potential solutions, one for every input O/F value. This total massflow is then used to compute O/F at all points using Eq. (22). The calculated O/F values are compared to the O/F range, eliminating all but a few valid solutions. An O/F guess (either the average burn O/F or the frame's previous O/F estimate if the loop iteration>1) is compared to the viable solutions. The nearest massflow value is selected. An example selection is illustrated in Figure 21. All possible solutions lie on the 1*O/F line. Solution 3 is selected, because it is the nearest point of intersect to the guess of the Computed O/F values and the solution line. The massflow solution is highlighted in blue.

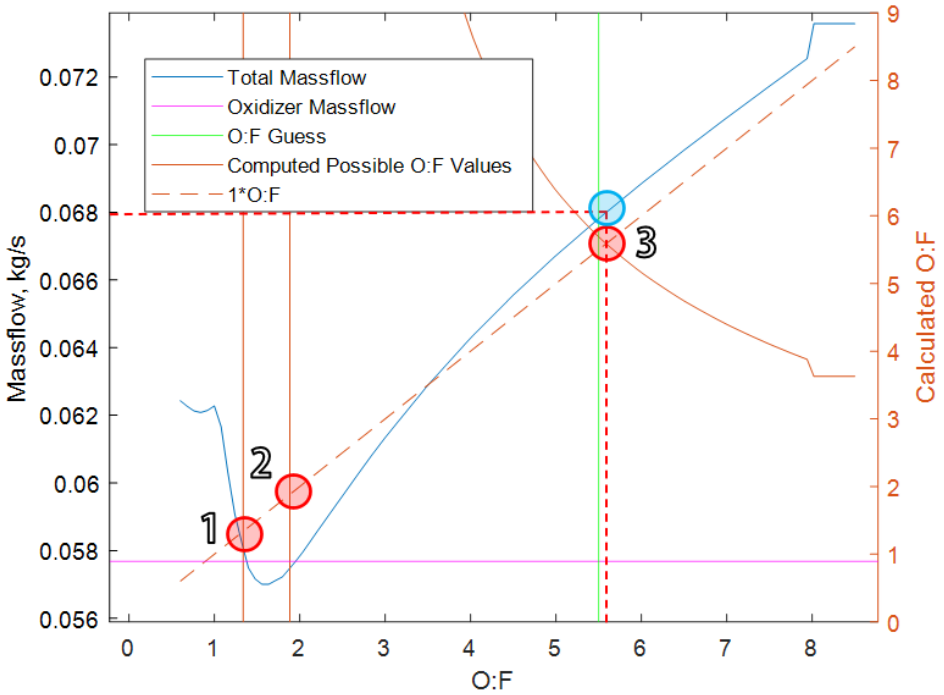

Figure 21: Example Massflow Estimate for a Single Frame of Captured Data.

Using this method for all points in time produces a massflow and O/F dataset with respect to time. The massflow estimates must be anchored by the measured total fuel consumed. The entire dataset is iterated until total estimated consumed fuel is equal to the motor mass pre-test minus the motor mass post test. Between each loop, combustion efficiency is modified, which has the primary effect of shifting the CEA flame temperature predictions. This efficiency modification is important, as previous USU research has shown CEA overestimates ABS/GOX temperatures at high O/F [35]. The final massflow data is used, in turn, to derive motor performance data with compressible fluids Eqs. (23)-(29) [37] [38]:

$$\frac{A_{exit}}{A_{throat}} = \left(\frac{\gamma+1}{2}\right)^{-\frac{\gamma+1}{2(\gamma-1)}} \frac{\left(1+\frac{\gamma-1}{2}M_{exit}^2\right)^{\frac{\gamma+1}{2(\gamma-1)}}}{M_{exit}} \tag{23}$$

$$T_{exit} = \frac{T_0}{1+\frac{\gamma-1}{2}M_{exit}^2} \tag{24}$$

$$P_{exit} = \frac{P_0}{\left(1+\frac{\gamma-1}{2}M_{exit}^2\right)^{\frac{\gamma}{\gamma-1}}} \tag{25}$$

$$V_{exit} = M_{exit}\sqrt{\gamma R_g T_{exit}} \tag{26}$$

$$F_{P0} = \dot{m}_{total}V_{exit} + A_{exit}\left(P_{exit} - P_{inf}\right) \tag{27}$$

$$I_{total} = \int_{t=end}^{t=0} F_{P0}\,dt \tag{28}$$

$$I_{sp} = \frac{F_{P0}}{g_0\dot{m}_{total}} \tag{29}$$

2.2 Test Campaign

The final test campaign was modified as the project progressed in order to accommodate the initial motor failure and the iterative design process. Table 2 lists the burns that took place as part of the test campaign.

Table 2: List of Hot-Fires Performed in Test Campaign

Burn #	Date	Test Description	Duration (s)	Notes
1	08/31/23	0% Vortex Characterization	8	Failure to Ignite
2	08/31/23	100% Vortex Characterization	7	Case Burnthrough, Loss of Motor
3	10/18/23	0% Vortex Ignition, Facility Verification	3	Nominal
4	10/19/23	0% Vortex Characterization	10	Nominal
5	10/27/23	0% Vortex Characterization	5	Initially Stuck Solenoid Valve, No Ox Massflow Data
6	10/27/23	0% Vortex Characterization	5	Nominal
7	10/27/23	50% Vortex, 0.333s Period, Characterization	5	Nominal
8	11/09/23	100% Vortex Characterization	5	Nominal
9	11/21/23	50% Vortex, 1s Period, Thrust Equalization	5	Initially Stuck Solenoid Valve
10	11/21/23	50% Vortex, 1s Period, Thrust Equalization	5	Late Ignition, Otherwise Nominal
11	12/01/23	100% Vortex Adjusted Orifice Characterization	10.25	Nominal
12	12/12/23	0.333s Period, Open Loop Control Attempt	10.25	Nominal
13	12/13/23	1s Period, Open Loop Control Attempt	10.25	Nominal
14	12/15/23	1s Period, Open Loop Control Attempt	10.25	Nominal

CHAPTER 3

RESULTS

3.1 Introduction

This section presents the results of the test campaign described in Chapter 2. The campaign successfully:

- Characterized the behavior of the baseline motor with axial injection.
- Identified the orifice sizing adjustments necessary for thrust equalization.
- Equalized steady-state thrust between axial and vortex injection.
- Characterized the behavior of 100% vortex injection with adjusted orifices.
- Developed an open-loop control scheme using characterization data.
- Achieved a target average O/F using open-loop control.

3.2 Characterization Burns

3.2.1 Burn 4, Baseline Axial Injection

Figure 22: Axial Characterization Burn Exhaust Plume

Baseline characterization was performed with 0% vortex injection. Matching the data with the numerical model results in coefficients n=0.31, a=0.00013. The total fuel consumed is 108.5g, with an average O/F of 5.18.

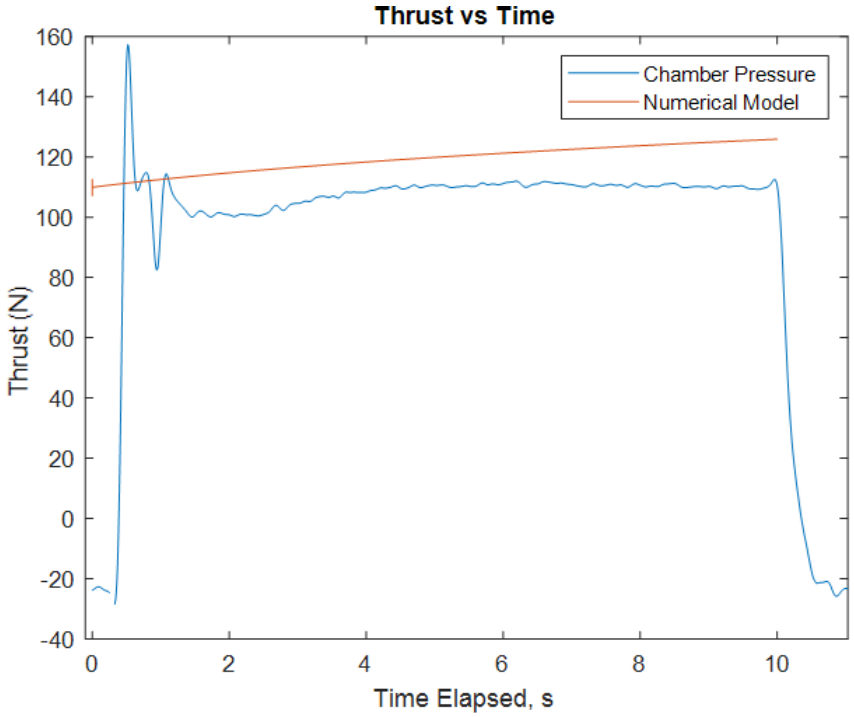

Figure 23: Axial Characterization Burn Thrust vs Numerical Model

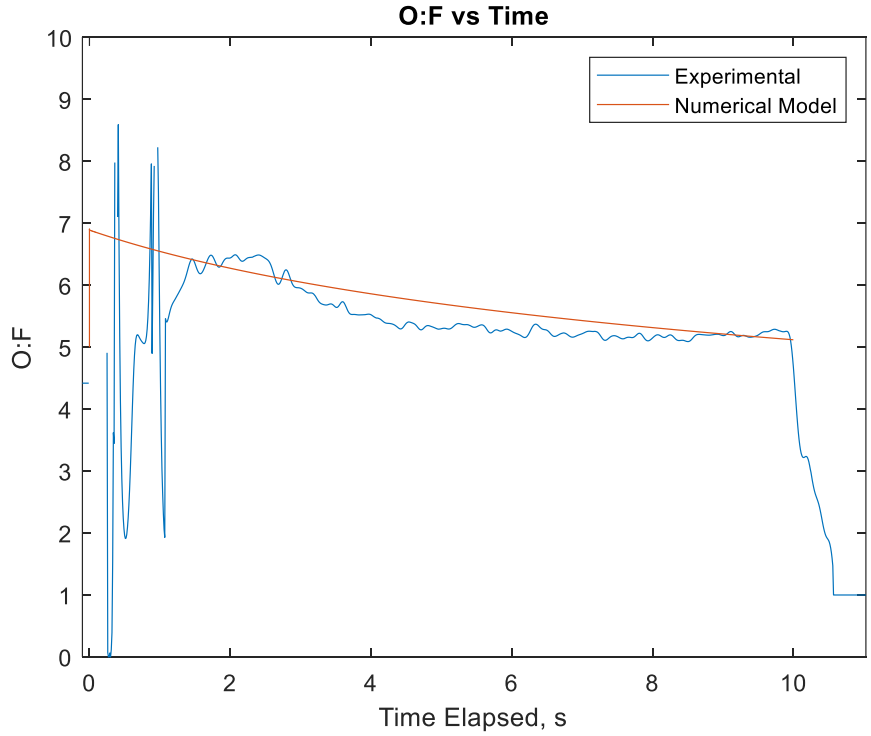

Figure 24: Axial Characterization Burn O/F vs Numerical Model

Figure 25: Axial Characterization Burn Fuel Grain Cross-Section

The profile of the axial injection fuel grain is consistent, non-erosive, and slightly smaller in diameter at midpoint. This is expected behavior and consistent with experience with previous USU motors.

3.2.2 Burn 11, 100% Vortex Injection

Figure 26: Vortex Characterization Burn Exhaust Plume

Vortex characterization was performed after burn equalization. The resulting performance was surprising in its complete departure from the behavior predicted by the numerical model in Chapter 1, where the numerical model predicted that vortex injection would result in a scaled curve similar in shape to axial injection (Figure 8), chamber pressure measurements suggest that vortex injection causes a positive burn exponent.

In order to achieve this profile in the numerical model, n=0.70, a=0.000037, S_g=50, and m=0.0005. The total fuel consumed is 233.5g, with an average O/F of 1.64.

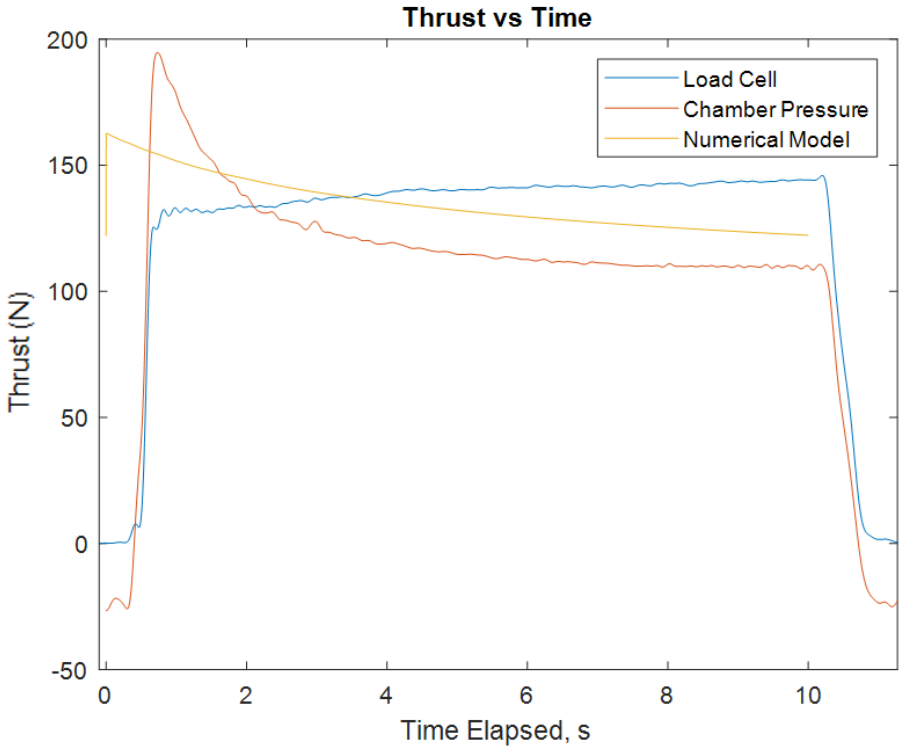

Figure 27: Vortex Characterization Burn Thrust vs Numerical Model

Load cell data is included in this plot to illustrate a theorized characteristic of vortex injection. The high spike in chamber pressure during startup may be the result of choking massflow due to the initial port diameter of 0.5in. Because vortex injection generates much higher massflow levels per unit oxidizer, particularly in the forward end, chamber pressure builds more quickly than it does during axial injection. The pressure transducer port is located in the forward end of the motor. This effect diminishes as the port diameter increases and the only potential choke point becomes the nozzle throat.

This theory is supported by the behavior of the load cell, which does not record the initial spike in thrust that chamber pressure suggests. The behavior, overall, is consistent with a choke point upstream of the nozzle caused by high forward-end massflux, which results in a spike in chamber pressure. The fuel grain burns back, moving any potential choke points aft until reaching the nozzle. Note that load cell data is only evaluated qualitatively.

If true, the vortex flow thrust estimates during startup are likely overestimates, while the calculated O/F is likely lower than reality.

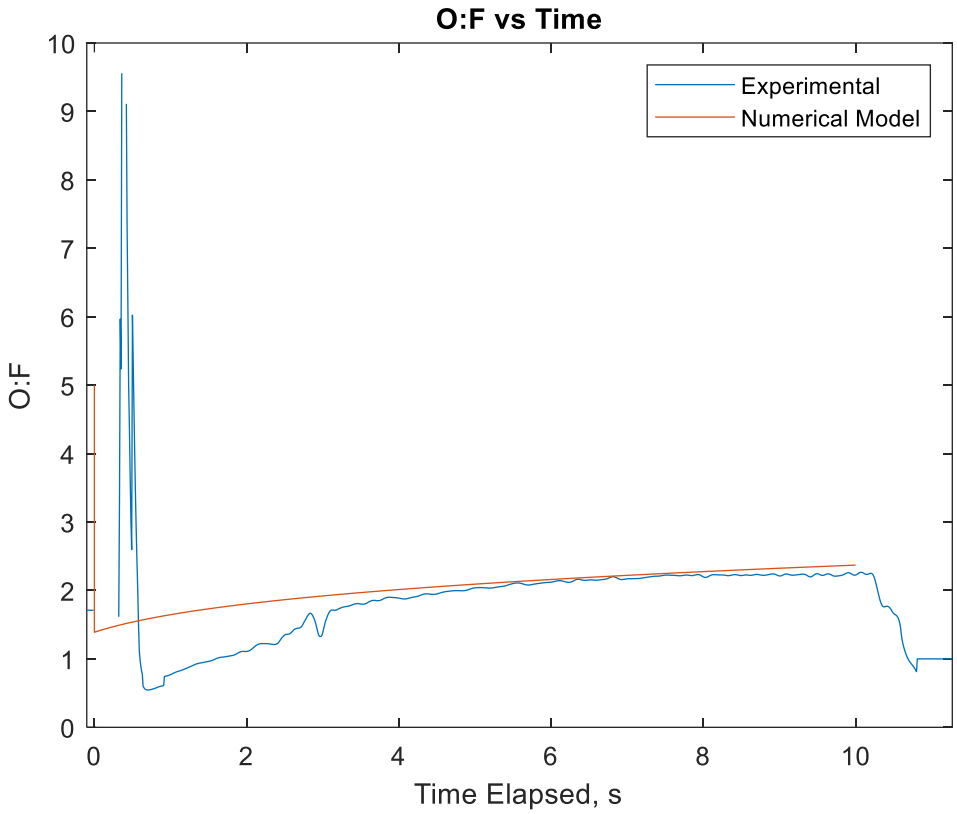

Figure 28: Vortex Characterization Burn O/F vs Numerical Model

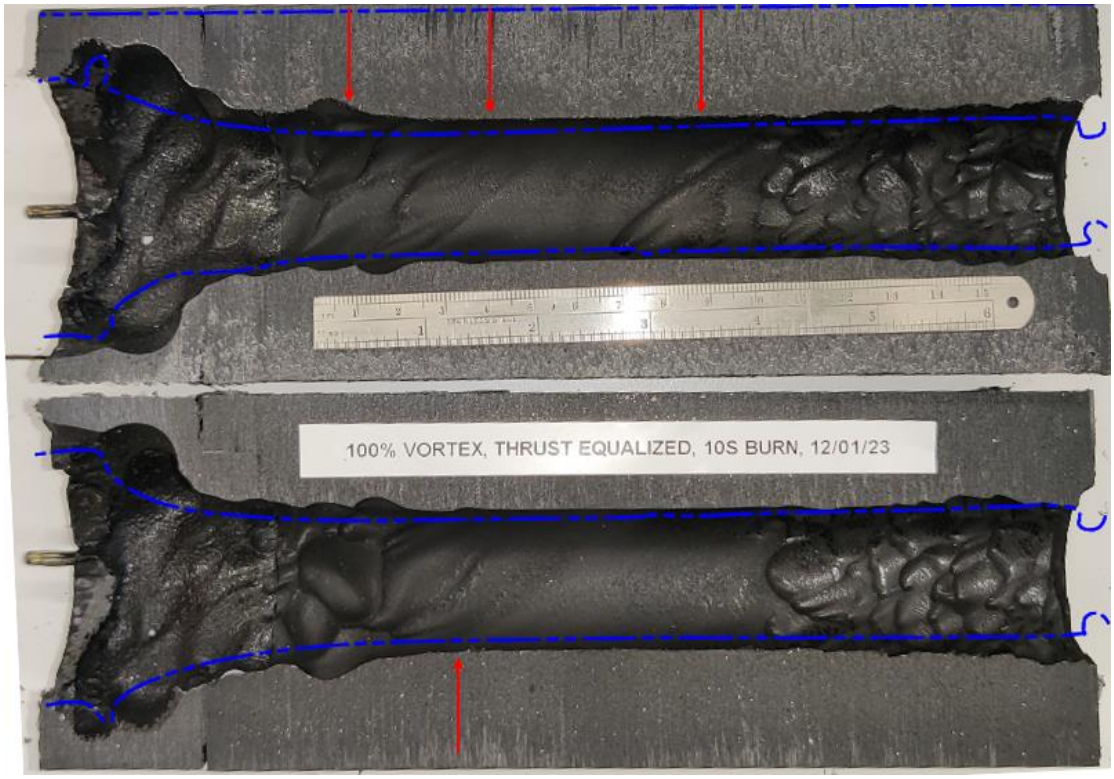

Figure 29: Vortex Characterization Burn Fuel Grain Cross-Section

The cross-section of the vortex-injection fuel grain is significantly different from that of axial injection. While total oxidizer consumption was less than that of the axial burn (burn 4), overall fuel consumption is greater. This indicates a decrease in O:F ratio. The vortex profile exhibits more forward-end burning and erosive burning. The erosive burning is indicative of high velocity gasses in the combustion chamber. Because total massflux after thrust equalization is similar to the axial injection grain, it can be concluded that higher-velocity flow in the chamber is the result of vortex flow. Note the red arrows in Figure 29 indicating streaks suggesting swirling flow. Also note the blue outline, which is an overlay of the axial fuel grain profile (Burn 4).

3.2.3 Effects of Vorticity

The characterization burns revealed vorticity to have a significantly greater impact than numerical modeling predicted. When total massflow is equalized between the two injection methods, $\frac{\text{Axial O/F}}{\text{Vortex O/F}}$=3.16. The result is more potential control authority than anticipated, and a wider application range than would have been possible with a smaller proportional effect.

3.3 Thrust Equalization

Thrust equalization began with an initial vortex burn where orifices were sized to target equal oxidizer massflow between axial and vortex injection. After collecting thrust data, assumed to be analogous to total massflow, orifices were swapped according to Figure 18. A verification burn was then performed to ensure that steady state thrust was equal for the two injection modes.

3.3.1 Burns 6 and 8, Pre-Equalization Thrust Characterization

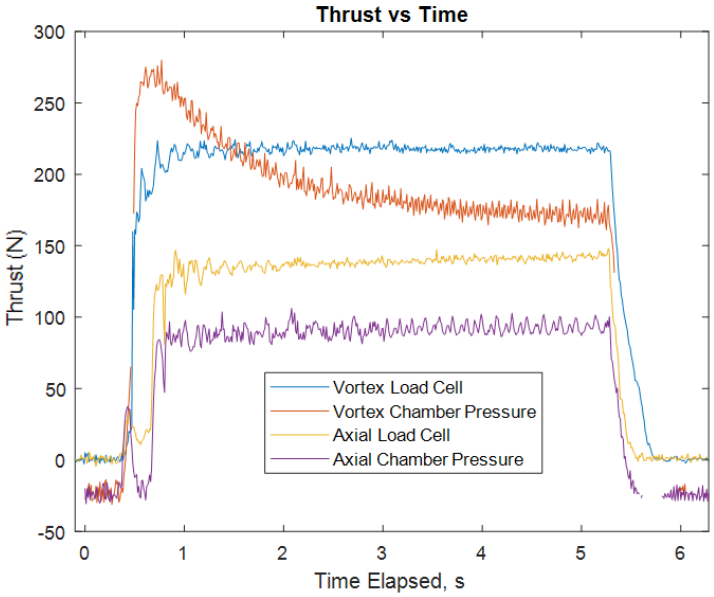

Figure 30: Pre-Equalization Vortex Characterization, Thrust vs Time

These burns provided the information necessary to swap to thrust-equalizing orifices, targeting $\dot{m}_{ox\_vortex} = 0.61\dot{m}_{ox\_axial}$.

3.3.2 Thrust Equalized Comparisons

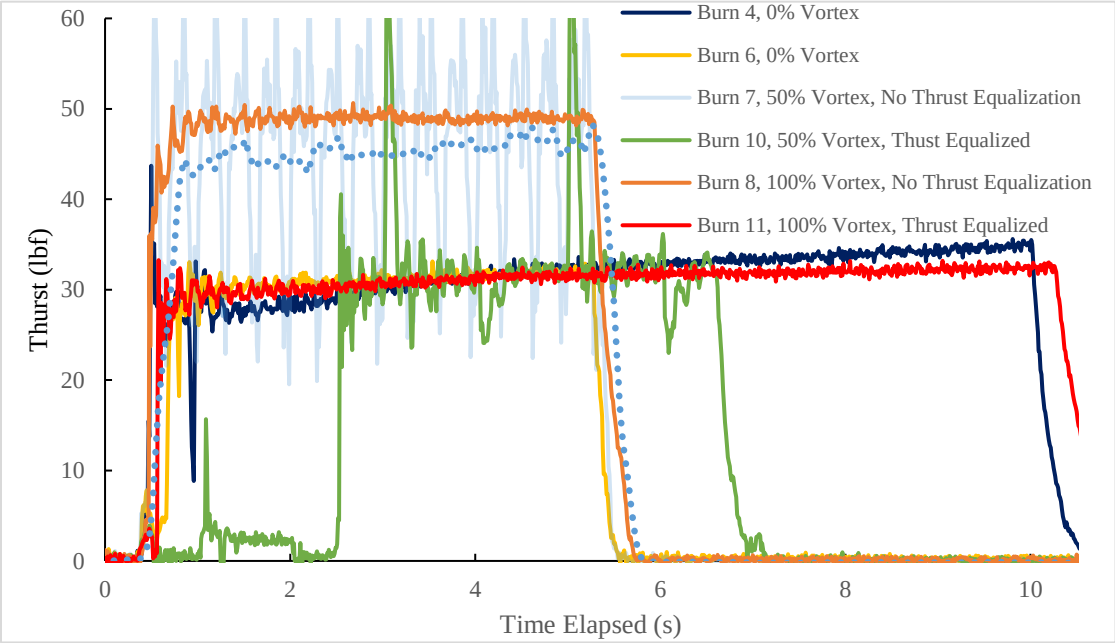

Figure 31: Thrust Equalization Comparisons

Figure 32: Burns 9 and 10 Fuel Grain Cross Section

3.4 Open Loop Control Scheme

During the test campaign, the method for estimating O/F described in 2.1.5 Analysis and Modeling was not yet developed. Instead, a more simplistic method was used. Total fuel mass consumed was measured by the proportion of total impulse achieved up to each point in the burn, such that:

$$m_{fuel_t} = m_{fuel_{total}} \frac{\int_t^{t_0} F_{load} dt}{\int_{t_{end}}^{t=0} F_{load} dt} \tag{30}$$

$$\dot{m}_{fuel_t} = \frac{m_{fuel,t} - m_{fuel,t-dt}}{dt} \tag{31}$$

The resulting O/F data was used to compute open loop schemes to achieve target O/F values, where:

$$V_{ratio} = \frac{O_{Faxial} - O_{Ftarget}}{O_{Faxial} - O_{Fvortex}} \tag{32}$$

The vortex ratio curve is then input into the open loop control table shown in Figure 20, along with the desired period.

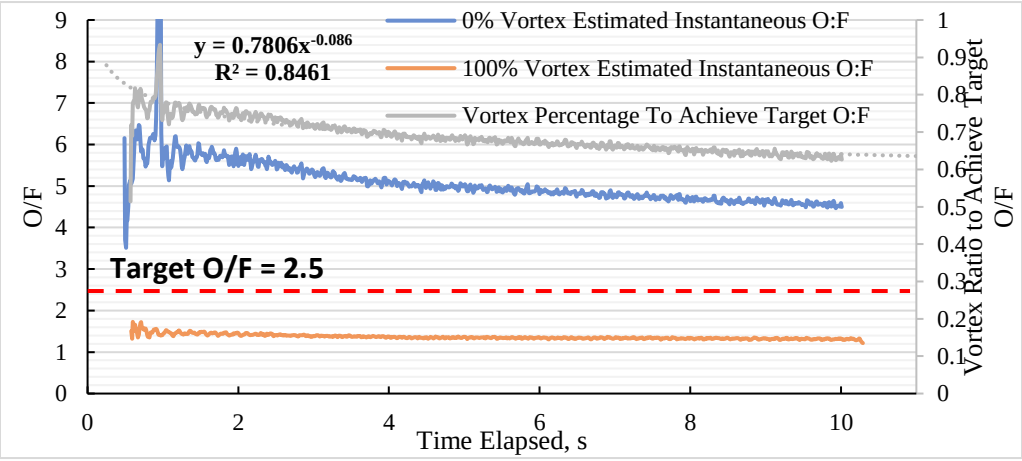

Figure 33: Open Loop Vortex Ratio Curve Using Impulse O/F Estimates

3.5 Open Loop Control Burns

3.5.1 Burn 12, 2.5 Target O/F, 0.333s Period

Figure 34: Burn 12 Exhaust Plume Comparison

The test campaign's first attempt at achieving a target O/F used a 0.333s period with a target of O/F=2.5. The valves actuated as commanded and the motor completed the burn. The oscillation caused by the pulse width modulation was violent, and extracting an accurate O/F estimate is not reliable. The transient behavior associated with switching between injections modes dominated the entire burn. In order to reduce oscillation and produce clearer data, subsequent burns used a longer period.

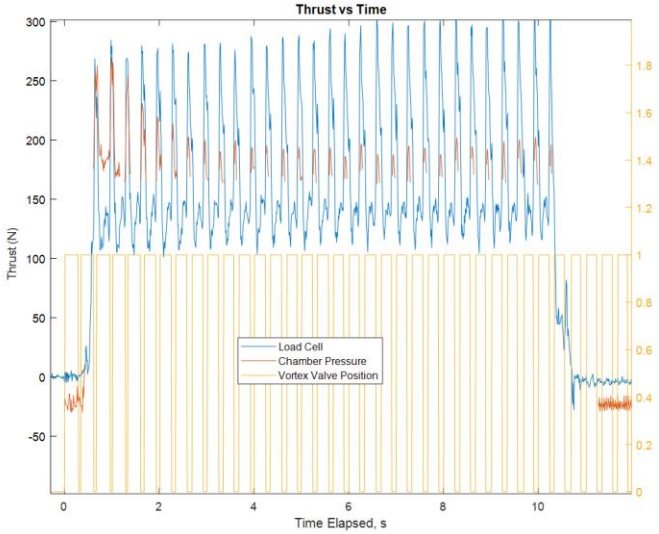

Figure 35: Burn 12 Thrust Data

Erosive burning was again found in the fuel grain cross-section. In this instance, the erosive burning appears to have taken place in the turbulent wake of the fiber-optic feedthrough near the center of the grain. The high frequency switch also increased the regression rate of the spark cap.

Figure 36: Burn 12, Fuel Grain Cross Section

3.5.2 Burn 13, 2.5 Target O/F, 1.000s Period

Burn 13, by comparison, was very successful, resulting in good data collection and a significant reduction in the strength of oscillations. The increased period allowed the transient conditions after switching to return to steady state. The total achieved O/F was 2.45, within 2% of the target value.

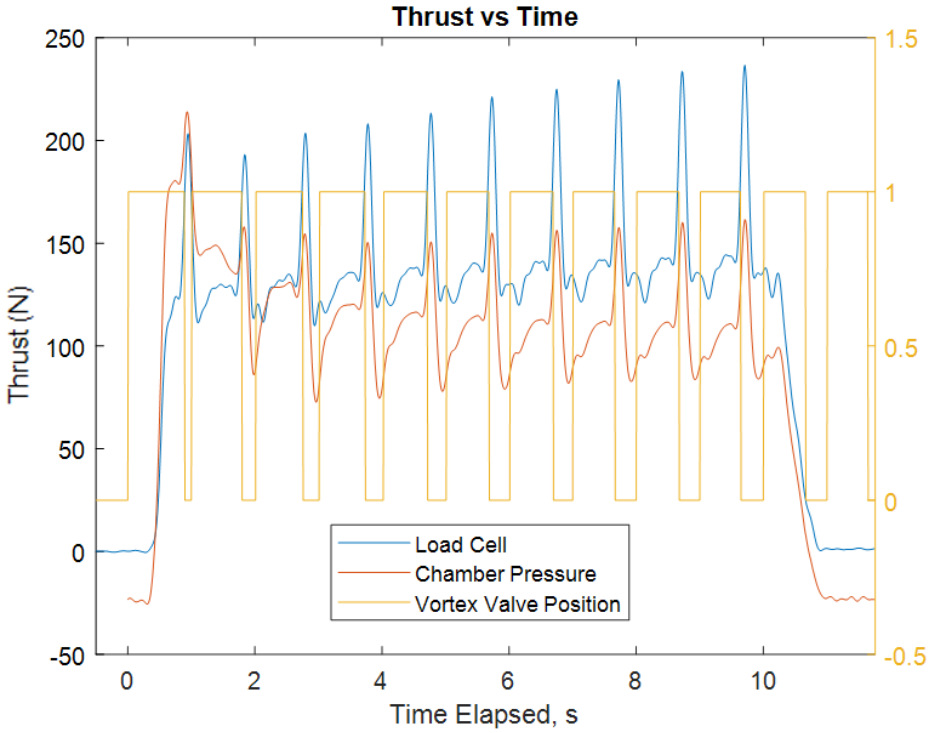

Figure 37: Burn 13, 2.5 Target O/F Thrust vs Time

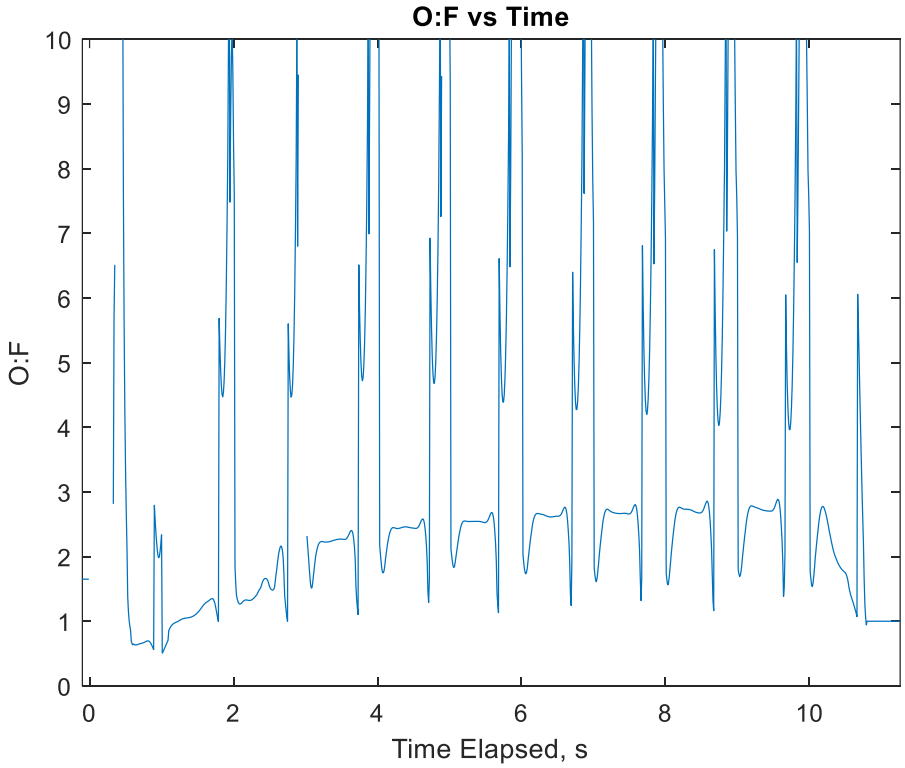

Figure 38: Burn 13, Estimated O/F vs Time

The transient behavior when valves switch is still present, but has a less disruptive impact than in Burn 12. After the initial startup transient, the average O/F is nearly constant with respect to time. As discussed in 3.2.2 Burn 11, 100% Vortex Injection, the accuracy of O/F and thrust estimates with vortex injection during startup may not be reliable. If the actual thrust follows the shape measured by the load cell (Figure 37), the motor likely achieved a constant O/F at ~2.5.

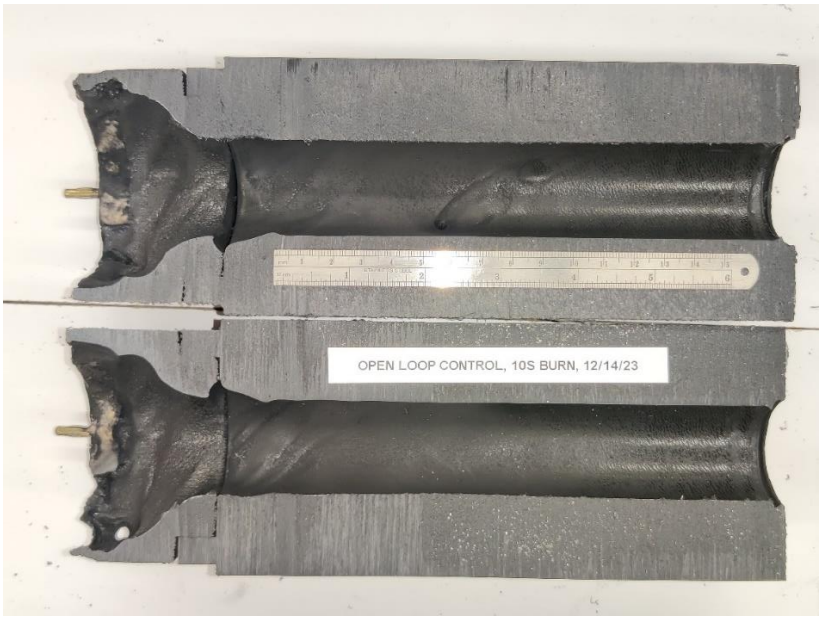

Figure 39: Burn 13, Fuel Grain Profile Cross-Section, Target O/F=2.5

In addition to achieving the target values, increasing the period to 1s had the effect of eliminating erosive burning in the fuel grain. Note that the port is nearly perfectly cylindrical, which is a desirable feature in order to increase the total lifetime of the motor. Overall, Burn 13 was an overwhelmingly successful demonstration of O/F manipulation.

3.5.3 Burn 14, 3.5 Target O/F, 1.000s Period

Burn 14 repeated much of the behavior of Burn 13. However, the achieved average O/F was 2.71, rather than the target 3.5. Similarly to Burn 12, the transient immediately following valve switching dominates each period. Because Burn 14 has shorter vortex dwell times, and the transient in vortex flow is longer than the transient in axial flow, the burn experienced less time at steady state conditions than Burn 13. The open loop scheme relies upon steady state conditions to achieve a target O/F. The accuracy would likely improve with a longer period, similar to the solution implemented after Burn 12.

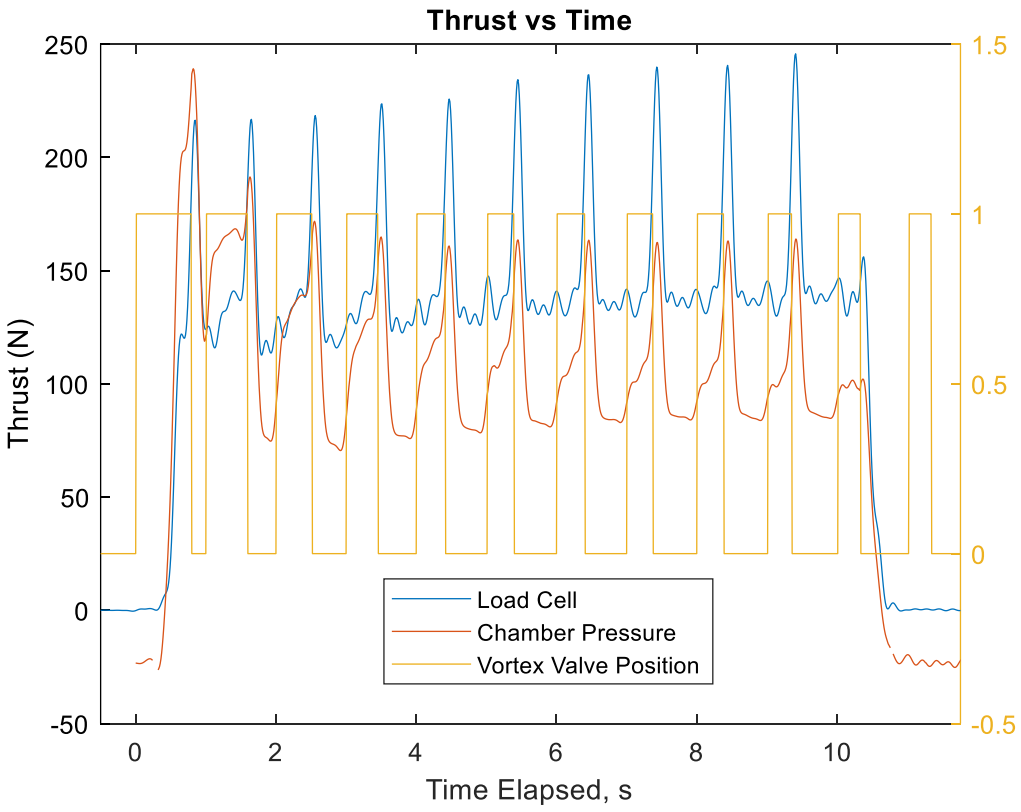

Figure 40: Burn 14, 2.5 Target O/F Thrust vs Time

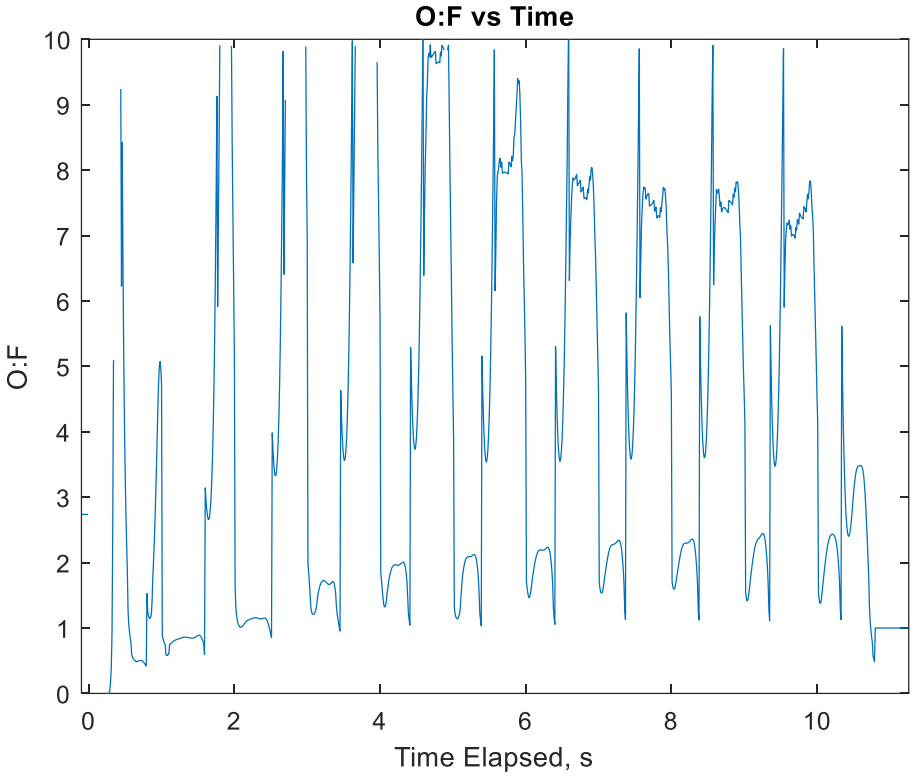

Figure 41: Burn 14, Estimated O/F vs Time

Figure 42: Burn 14, Fuel Grain Profile Cross-Section, Target O/F=3.5

Erosive burning is again observed in Burn 14. If this is the result of the proportional time spent during a burn in transience after valve switching, increasing the period could reduce or eliminate erosion.

3.6 Transient Response to Valve Actuation

Reaching steady state after switching injection modes is not instantaneous. The time between the switch and steady state is the transient. The transient was observed to have a large and undesirable effect on motor performance and controllability during the test campaign. Increasing the pulse width modulation period, as seen in 3.5, helps overcome the effects of the transient by reducing the proportion of time that the motor is in a transient state.

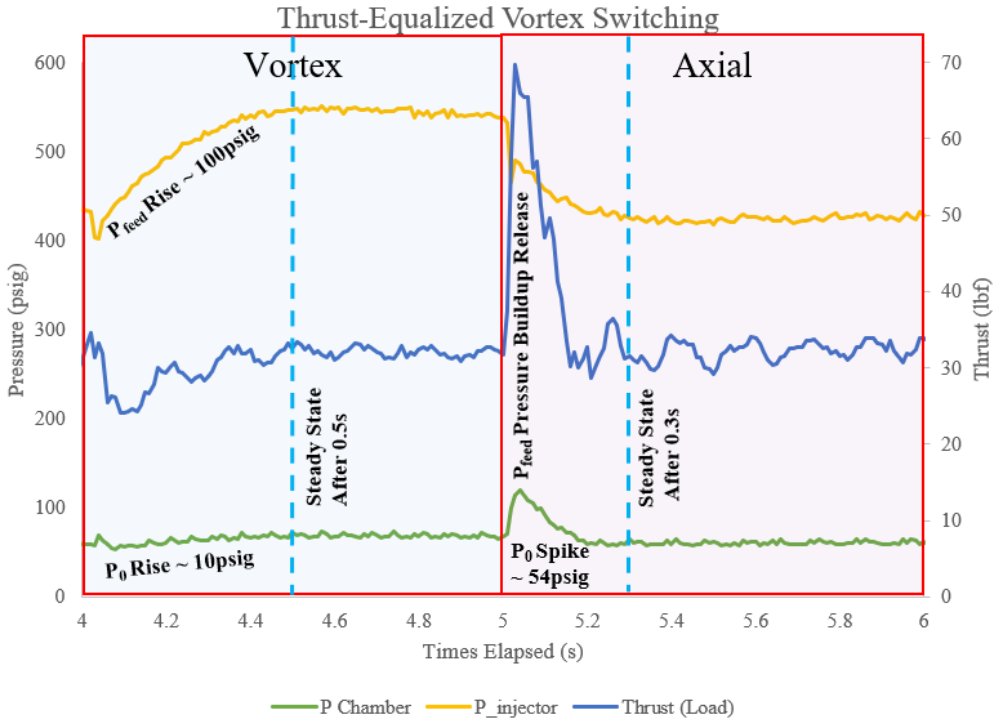

Figure 43: Transients Following Vortex and Axial Switching

Transience is primarily driven by the injector feed pressure response to orifice sizing. The smaller vortex orifices drive a higher pressure differential across the injector than the larger axial orifice. When switching from Axial to Vortex flow, the injector feed line is underpressurized, requiring approximately 0.5s to rise the 100psi necessary to reach steady state injection. A corresponding rise in chamber pressure and thrust follow. Conversely, when switching back to axial injection, the feed line is over pressurized. The excess pressure is released through the now larger orifice, quickly causing a spike in chamber pressure, thrust, and O/F. Mechanical oscillations, suboptimal O/F, and erosive burning result from transients.

Eliminating this transient behavior is desirable for increased controllability of the motor. This could be reliably achieved by installing a check valve at each injector feed line immediately downstream of a choked throttle valve, preventing pressure feedback from reaching the opposite valve during switching.

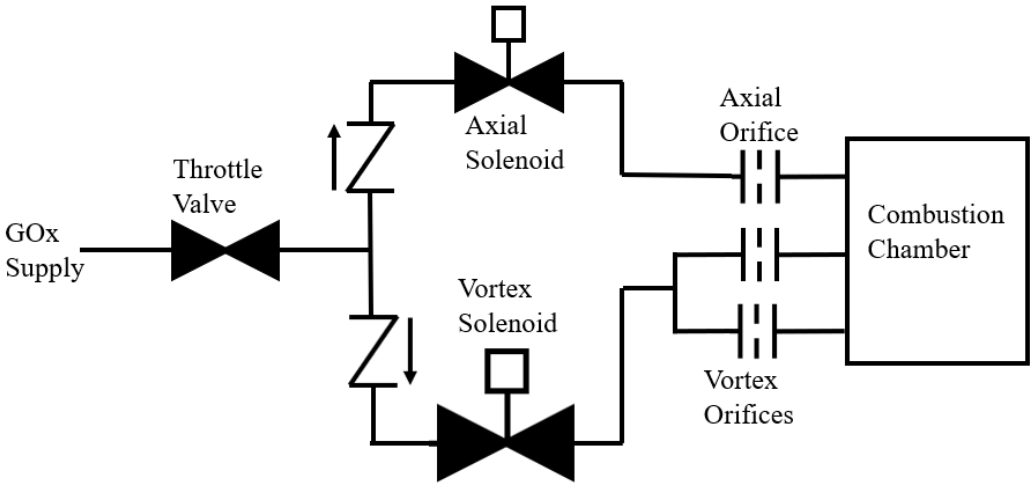

Figure 44: P&ID Diagram for Injector Feedback Mitigation

3.7 Efficiency

A primary goal of O/F manipulation is to increase the efficiency of a rocket motor. As discussed in 1.2.1, the optimal O/F value for an ABS/GOX hybrid is ~1.5. The test campaign results reinforce this numerical prediction. Figure 45 displays selected specific impulse(Isp) profiles from the test campaign. The highest average Isp is achieved in burn 11, with an average O/F of 1.64. As the average O/F increases, average Isp decreases, consistent with characteristic velocity predictions in Figure 1. Vortex injection, in this motor, increased average specific impulse by 25% over the baseline axial injection.

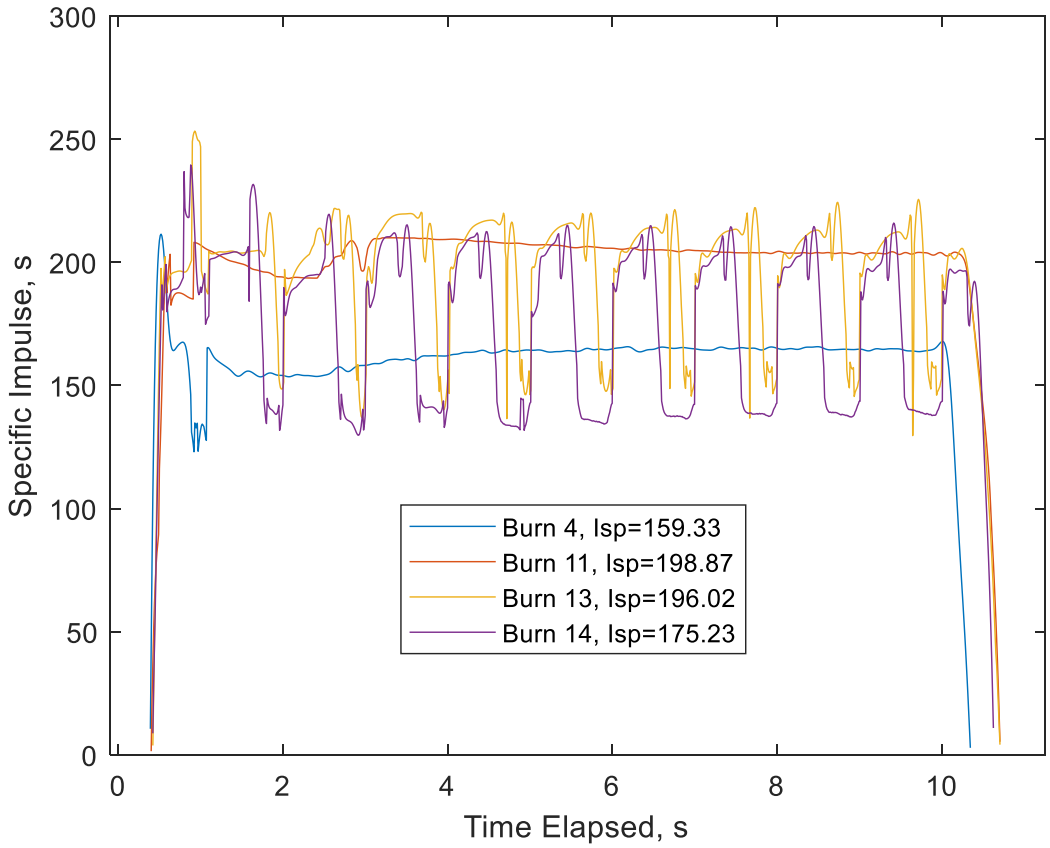

Figure 45: Specific Impulse for Selected Burns

CHAPTER 4

SUMMARY

This thesis project has sought to develop a hybrid rocket motor capable of O/F shift manipulation via vortex strength control. After an iterative design process, the project developed a robust swirl motor and control mechanism. The O/F profiles for axial and vortex injection were observed and quantified, revealing that vortex injection has a large effect on combustion behavior, increasing fuel regression rate per unit oxidizer by over three times. This data was used to resize injector orifices, matching total exhaust massflow and thrust for vortex injection to that of axial injection. The result of this thrust equalization is vortex control independent of throttle.

Vortex injection dramatically reduces O/F. In this motor, a sustained 100% vortex burn over 10s results in an average O:F of less than 1/3 that of a comparable 0% vortex burn. The magnitude of O:F control demonstrated by these results exceeds expectations and makes possible greater controllability than hoped for based on numerical predictions. This validates the central working principle of the thesis and makes possible many potential applications.

The O/F profiles of the two injection modes were then used to develop an open loop control scheme for O/F compensation. Upon implementing the open loop control scheme, it was discovered that the transient injector feed pressure limits the effective frequency of pulse width modulation. Despite this limitation, the motor successfully achieved a target O/F within 2% of the goal over a 10s burn, accomplishing the main objective of this thesis project and setting the stage for future work.

Hybrid rocket motors offer a wide range of potential benefits to spaceflight missions. Hybrids boast features such as “green” propellants, low complexity design, high theoretical efficiency, the ability to be deeply and quickly throttled [39], and multiple low-energy restarts [29]. As robotic and human spaceflight proliferates, these abilities have the potential to enable a wide range of missions. Hybrids are handicapped, however, by variable combustion properties that force a number of compromises that ultimately slow their adoption. O/F shift compensation eliminates the combustion variability that otherwise hinders hybrid motor implementation.

Properly implemented, the O/F manipulation proven possible by this thesis can be used to control hybrid motor time-impulse distribution, greatly increase overall hybrid efficiency, increase the lifespan of non-consumable motor components for reusability, allow for a wide range of mission profiles in a single configuration, and significantly reduce the cost of missions that would otherwise use alternative propulsion systems.

The success of this O/F control methodology proves hybrids can be the versatile and transformative system that the features described above suggest. Hybrids can, therefore, be effective and relatively low-cost solutions for lab high-enthalpy gas generation, Mars and Lunar sample return, smart upper stages, ascent and descent stages, station-keeping, de-orbit, orbital insertion, and potentially many more critical applications.

CHAPTER 5

FUTURE WORK

The achievements of this project are far from the upper limits of this technology's application. While pulse width modulation helped this project use time and funds more efficiently, the configuration is not well-suited for optimal motor performance. Continuous or high-resolution throttle control for each injection method would eliminate transient considerations, mechanical oscillations, and efficiency losses associated with the individual injection methods (example, neither injection method produces an exactly optimal O/F). This flow control method would allow more flexible open and closed loop control schemes.

Closed loop control represents a major potential improvement to the system. While the O/F estimates in this project use a post-mass measurement to anchor massflow calculations, a real-time O/F estimation method is possible. USU has already demonstrated the ability to measure flame temperature using spectroscopy [7,40]. If refined to operate in real time, closed loop control would significantly increase the versatility of the system. Other real-time O/F measurement methods would also enhance the system's capabilities.

Using closed loop control to vary simultaneous flow rates of the two injections modes has the capacity to dramatically increase the versatility of this technology. Obstacles related to erosive burning, switching transients, and performance uncertainty would be effectively eliminated. This technology upgrade represents the potential

difference between a lab research motor and the application of this system to enable otherwise impossible or impractical spaceflight missions.

Forward end motor geometry can also be improved. Currently, the graphite dispersion ring has limited lifespan because of direct oxidizer impingement. Other materials, such as annealed pyrolytic graphite, boron nitride, etc. may increase forward-end lifetime. Other geometries that reduce the regression rate of the ignition system may also be considered.

Finally, this project used only a single impeller geometry for all vortex injection. There is no direct evidence that this impeller geometry (pitch likely being the most relevant factor) is the best possible configuration. The farthest extent of this concept may be a variable-pitch impeller, which would eliminate the need for multiple injection methods.

The abilities demonstrated and the concepts validated by this technology are transformative for hybrid rocketry if properly developed and implemented into a flight motor. The future work building off this project should be pursued to fully take advantage of the many benefits made possible by this technology.

APPENDICES

APPENDIX A

FLAME TEMPERATURE MEASUREMENTS

Table 3: Spectroscopy-Derived Baseline Flame Temperatures for Selected Burns.

Burn #	Blackbody Curve Fit Temperature, K	Wein's Law Temperature, K
4	2823.23	2821.90
5	2904.45	2904.4
8	2854.79	2852.64
9, Axial	2531.38	2529.56
9, Vortex	2739.49	2738.75
10, Vortex	2875.76	2875.41
11	2838.01	2835.79
12	2802.38	2799.97
13	2768.22	2767.69
14	2771.08	2770.35

APPENDIX B

INITIAL HARDWARE DESIGN FAILURE

The initial hardware design configuration resulted in a motor failure and major redesign. The original design, motor failure, and failure investigation are detailed in this section.

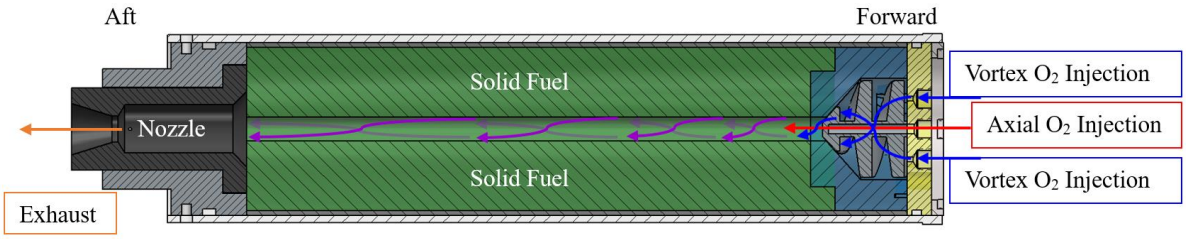

Figure 46: Initial Design Concept Cross Section

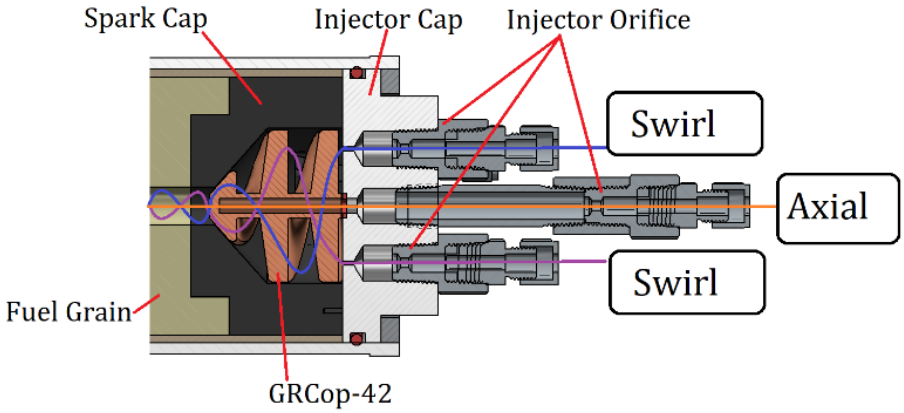

Figure 47: Initial Design Injector Cross Section

Initial attempts to begin the motor testing campaign were frustrated by multiple design flaws. The first burns of the test campaign were planned to be baseline axial injection burns used to characterize the behavior of the motor in the traditional hybrid

configuration. Burns were performed without incident without the GRCop-42 impeller installed. Subsequently, the impeller was installed and the following attempts to fire the motor resulted in ignition failures (flowing oxidizer with no flame). After multiple attempts, it was determined that. The inability to ignite the motor with USU's traditionally reliable ignition system [29] was the result of two primary factors.

1. The G10 insulators around igniter electrical feedthroughs were charred by the previous burns, creating a low impedance short that prevented current from reaching the intended igniter lead ends. This short was observed directly by personnel while energizing the spark igniter while disassembled. This issue was bypassed in the initial by removing the carbon buildup before testing.

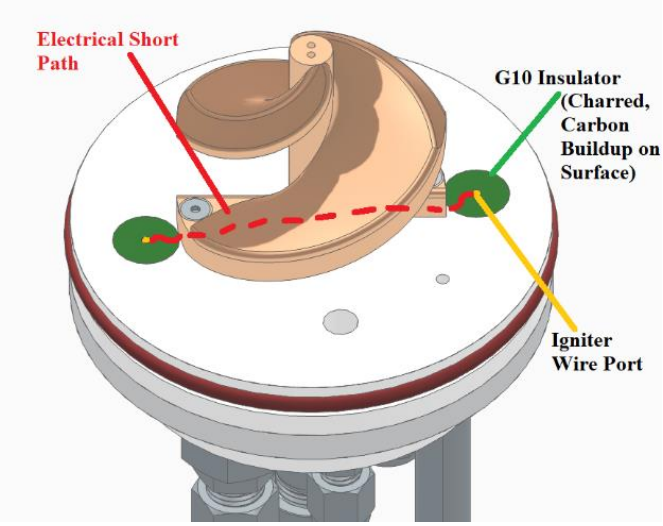

Figure 48: Igniter Short Path

2. The impeller likely created flow restriction preventing sufficient oxidizer from circulating passed the spark. This theory is supported by the inability to light the motor via axial injection while experiencing no difficulty later igniting with vortex injection.

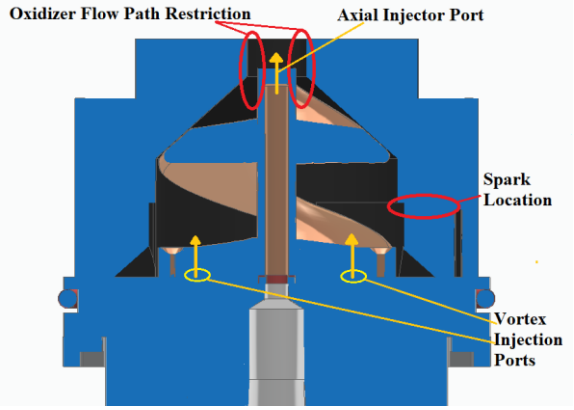

Figure 49: Igniter Flow Path Restriction

Unable to ignite the motor with axial flow, the test campaign shifted to a vortex flow burn. The motor ignited properly and burned for ~7s. Within the first second after ignition, the exhaust plume was tinted green, indicating vaporized copper was exiting the nozzle.

Figure 50: Green Exhaust Indicating Vaporized Copper. 0s<T<1s.

At ~T+7s, the motor failed via a case burn through immediately downstream of injector. This resulted in a loss of the motor.

Figure 51: Motor Burnthrough with Debris

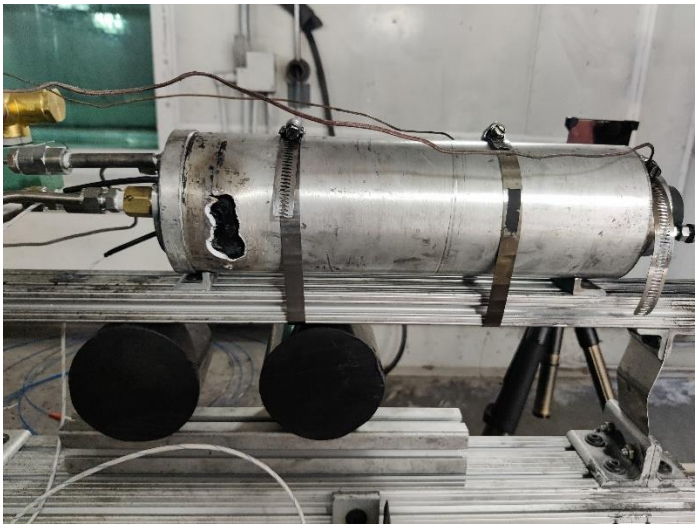

Figure 52: Damaged Case After First Iteration Burnthrough

A failure investigation found that the chamber experienced expected chamber pressures during the burn, but that the forward end of the motor was extensively damaged. In addition to the damage to the case and liner, the impeller was mostly consumed, the igniter electrical feedthroughs burned back, and the spark cap disproportionally and asymmetrically consumed compared to the fuel grain and previous burns. In previous tests with the legacy motor, the highest regression rates occurred at the aft end of the motor.

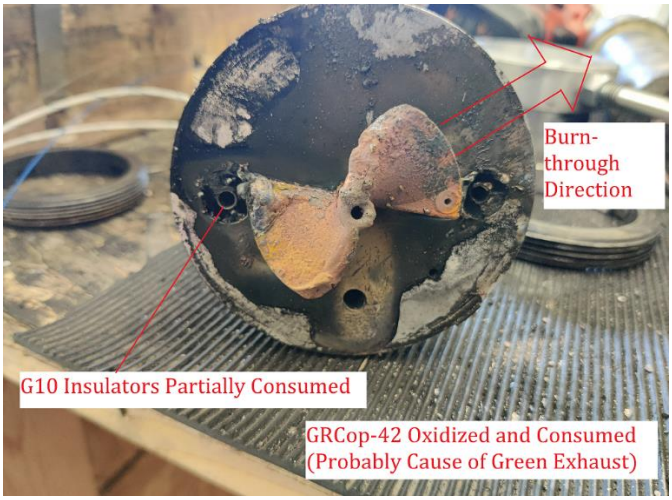

Figure 53: Injector Damage Post-Burnthrough

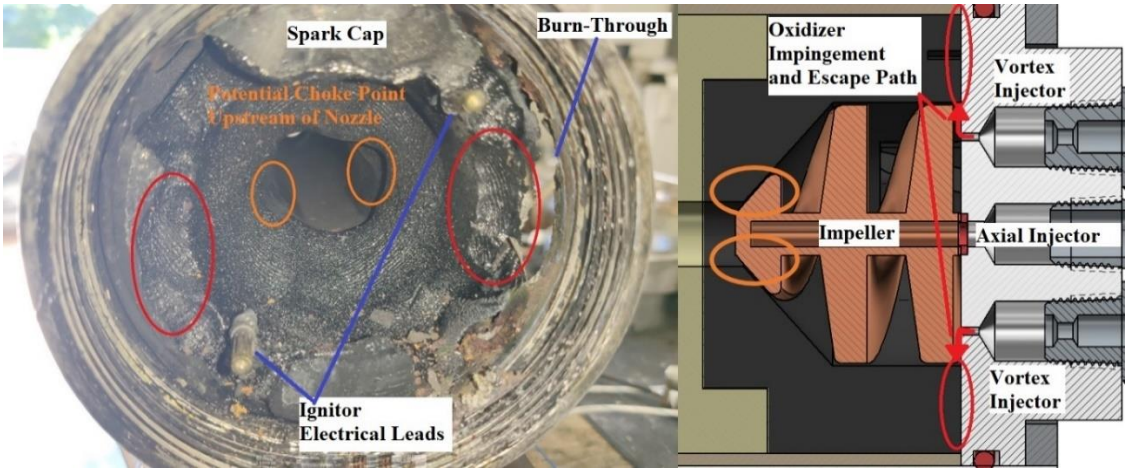

Figure 54: Spark Cap Asymmetric Regression with Locations in CAD Model

The failure investigation established a chain of causes and effects leading to the motor failure as follows:

1. Oxidizer deflects off of impeller surface immediately after entering the chamber, impinging directly onto the surface of the spark cap.
2. Forward-end gas generation, as a result, increases significantly compared to axial injection in a traditional configuration.

3. Now-increased exhaust massflow chokes near the aft end of the impeller.
4. Flow stagnation prevents oxidizer cooling of impeller and results in rising forward-end temperature.
5. As material burns, available fuel surface area increases, resulting in positive feedback.
6. Thin walls of spark cap are completely consumed, exposing the phenolic liner and chamber wall directly to flame
7. Liner and case cannot withstand flame temperature and are burned/melted away.

These findings necessitated an injector re-design to eliminate the causes of the failure from future burns. The redesign must increase ignition reliability, eliminate chokepoints upstream of the nozzle, and prevent concentrated oxidizer impingement on spark cap walls.

First, to address ignition and injector lifetime issues, the G10 feedthrough insulators were replaced with boron nitride [30], which prevents charring and burn back (Figure 57). This was effectively a drop-in replacement. Ignition reliability is also affected by the oxidizer backflow to the spark. In response, the vortex generator (impeller) profile was significantly reduced.

Second, additional chokepoints upstream of the nozzle were eliminated. No point in the injector downstream of combustion has a cross-sectional area small enough to choke flow at the relevant pressure differentials.

Third, the spark cap wall thickness was increased as far as possible while accommodating the injector redesign. This grants additional reaction time to test operators and generally increases the life of the motor.

Fourth, and most critically, the redesign significantly reduced the concentrated impingement of un-combusted oxygen on any surface downstream of combustion by implementing a dispersion ring in the injector assembly, which serves to distribute oxidizer flow more evenly along the circumference of the port before contacting the spark cap (Figure 16). Multiple materials were considered for production of the impeller and dispersion ring, including aluminum, brass, boron nitride, alumina 960, and graphite. Additive manufacturing was excluded because of prohibitive costs, eliminating GRCop-42 from the assembly. Multiple configurations were produced and tested, resulting in individual component failures (see example in Figure 56). Ultimately, the final motor uses machined graphite [31] for both the impeller and dispersion ring, accomplishing all re-design objectives. Figure 58 compares the completed initial design and final design.

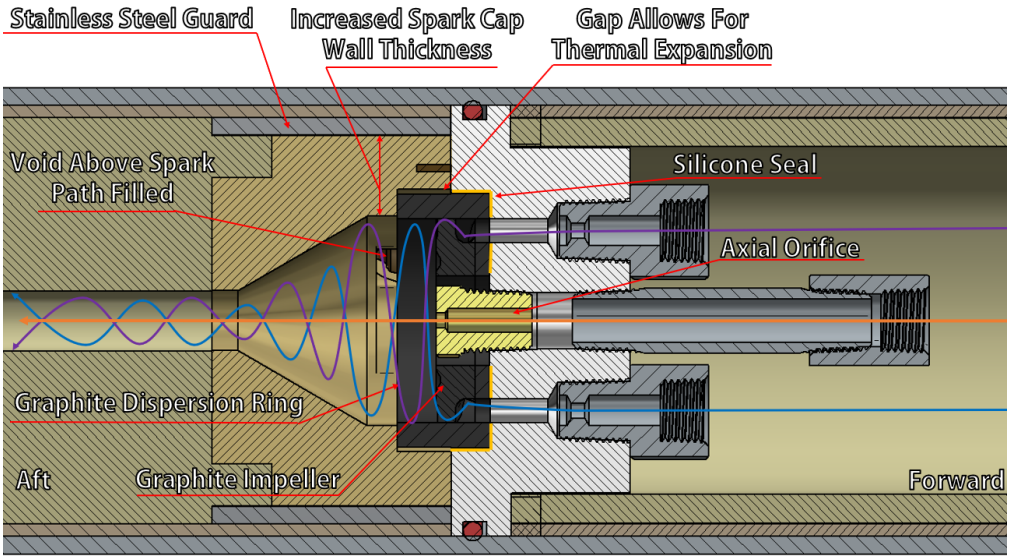

Figure 55: Injector Re-Designed Features Cross-Section

Figure 56: Post-Test Shattered Alumina 960 Dispersion Ring

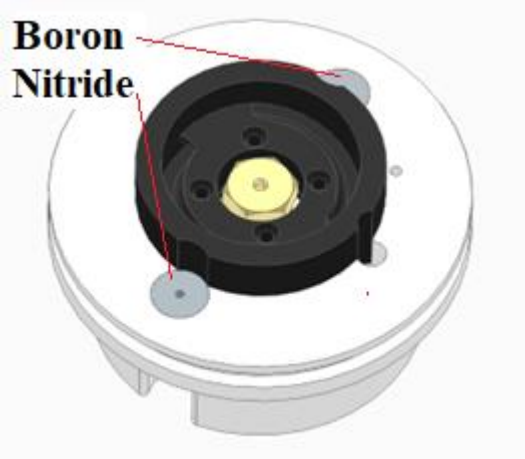

Figure 57: Injector Re-Design Isometric View

Figure 58: Initial Build (Left) Compared to Final Build (Right)

REFERENCES

[1] Anon., “Hazard Analysis of Commercial Space Transportation; Vol. 1: Operations, Vol. 2: Hazards, vol. 3: Risk Analysis,” U.S. Dept. of Transportation, PB93-199040, Accession No. 00620693, May 1988. https://www.faa.gov/about/office_org/headquarters_offices/ast/.../hazard.pdf

[2] Dornheim, M. A., “Reaching 100 km,” Av. Week Space Technol., Vol. 161 No. 6, 2004, pp 45–46. https://www.researchgate.net/publication/292268464_Reaching_100_km.

[3] Casalino, L., and D. Pastrone. 2012. “Optimization of Hybrid Sounding Rockets for Hypersonic Testing.” J. Prop. Power, Vol. 28, No. 2, March-April 2012, pp. 405–411. https://doi.org/10.2514/1.B34218.

[4] Casalino, L., and D. Pastrone. 2008. “Optimal Design of Hybrid Rocket Motors for Microgravity Platform.” J. Prop. & Power, Vol.24 No. 3, May-June 2008, pp., 491–498. https://doi.org/10.2514/1.30548

[5] Jens, E., A. C. Karp, B. Nakazono, D. B. Eldred, M. E. DeVost, and D. Vaughan. 2016. “Design of a Hybrid CubeSat Orbit Insertion Motor.” AIAA 2016-4961, 52nd AIAA/SAE/ASEE Joint Propulsion Conference, Salt Lake City UT, 25-27, July 2016. https://doi.org/10.2514/6.2016-4961

[6] Casalino, L., and D. Pastrone. 2015. “A Straightforward Approach for Robust Design of Hybrid Rocket Engine Upper Stage,” In Proc., AIAA 2015-4202, 51st AIAA/SAE/ASEE Joint Propulsion Conf., Orlando FL, 27-29 July 2015. https://doi.org/10.2514/6.2015-4202

[7] Karp, A. C., B. Nakazono, J. B. Manrique, R. Shotwell, D. Vaughan, and G. T. Story. 2016. “A hybrid mars ascent vehicle concept for low temperature storage and operation.” AIAA 2016-4962, 52nd AIAA/SAE/ASEE Joint Propulsion Conference, Salt Lake City UT, 25-27, July 2016. https://doi.org/10.2514/6.2016-4962

[8] Stephen A. Whitmore, S. A., Peterson, Z. W., and Eilers, S. D., “Closed-Loop Precision Throttling of a Hybrid Rocket Motor,” J. Propulsion and Power, Vol. 30, No. 2, February 2014, pp. 325-336. https://doi.org/10.2514/1.B34924

[9] Whitmore, S. A., Spurrier, Z. S., Walker S. D., and Merkley, S. L., "Throttled Launch-Assist Hybrid Rocket Motor for an Airborne NanoSat Launch Platform,” AIAA 2016-4658, 52nd AIAA/SAE/ASEE Joint Propulsion Conference, Salt Lake City UT, 25-27, July, 2016. https://arc.aiaa.org/doi/abs/10.2514/6.2016-4658

[10] Whitmore, S. A., Inkley, N. R., Merkley, D. P., and Judson, M. I., "Development of a Power-Efficient, Restart-Capable Arc Ignitor for Hybrid Rockets", J. Propulsion and Power, Vol. 31, No. 6 (2015), pp. 1739-1749. DIO: https://dio.org/10.2514/1.B35595

[11] Whitmore, S. A., Mathias, S. D., and Harvey, R., “High Voltage Breakdown and Arc-Tracking Mechanism of Thermoplastics with Applications to Hybrid Rocket Arc- Ignition,” AIAA 2017-4601, 53rd AIAA/SAE/ASEE Joint Propulsion Conference, Atlanta, GA, 10-12 July 2017. https://doi.org/10.2514/6.2017-4601

[12] Stephen A. Whitmore, Stephen L. Merkley, Louis Tonc, and Spencer D. Mathias, "Survey of Selected Additively Manufactured Propellants for Arc Ignition of Hybrid Rockets", J. Propulsion and Power, Vol. 32, No. 6, Nov.-December, 2016, pp. 1494-1504. http://dx.doi.org/10.2514/1.B36106

[13] Whitmore, S. A., and Bulcher, A. M., "A Green Hybrid Thruster Using Moderately Enriched Compressed Air as the Oxidizer", AIAA 2018-4841, 2018 Joint Propulsion Conference, AIAA Propulsion and Energy Forum, Cincinnati OH, 9-11 July, 2018, https://doi.org/10.2514/6.2018-4841

[14] Betts, J. T., “Survey of Numerical Methods for Trajectory Optimization,” Journal of Guidance, Control, and Dynamics, Vol. 21, No. 2, Feb. 1998, pp. 193–207. https://doi.org/10.2514/2.4231

[15] Casalino, L., and D. Pastrone. 2013. “Integrated design-trajectory optimization for hybrid rocket motors.” In Modeling and optimization in space engineering, 343–363. New York: Springer. https://link.springer.com/chapter/10.1007/978-1-4614-4469-5_14.

[16] Kuo, K. K., Chiaverini, M. J., "Fundamentals of Hybrid Rocket Combustion and Propulsion, "Progression in Astronautics and Aeronautics," American Institute of Aeronautics and Astronautics, 2007, pp. 37-126, eISBN/ 978-1-60086-687-6, print ISBN/ 978-1-56347-703-4, DOI/ 10.2514/4.866876.

[17] Casalino, L., and D. Pastrone. 2016. “Optimal Robust Design of Hybrid Rocket Engines,” Optimization and its Applications, Springer Publishing, New York, 2015, pp. 269–285. http://dx.doi.org/10.1007/978-3-319-41508-6_10

[18] Casalino, L., Masseni, F., and Pastrone, D., " Uncertainty Analysis and Robust Design for a Hybrid Rocket Upper Stage," J. Spacecraft and Rockets, Vol. 56, No. 6, March 2019, pp. 1-8. DOI: 10.2514/1.A34422

[19] S. Gordon, B. J. McBride, Computer Program for Calculation of Complex Chemical Equilibrium Compositions and Applications, NASA, RP-1311, (1994). https://www.grc.nasa.gov/www/CEAWeb/RP-1311.htm

[20] Karabeyoglu, A. M., & Evans, B. J. (2014). Effect of "O/F shift" on combustion efficiency. *50th AIAA/ASME/SAE/ASEE Joint Propulsion Conference*. https://doi.org/10.2514/6.2014-3851

[21] Marxman, G. and Gilbert, M., "Turbulent Boundary Layer Combustion in the Hybrid Rockets," Symposium (International) on Combustion, Vol. 9, no. 1., 1963, pp. 371–383. https://doi.org/10.1016/S0082-0784(63)80046-6. (accessed 30 March, 2023)

[22] Marxman, G. A., Wooldridge, C. E., and Muzzy, R. J. "Fundamentals of Hybrid Boundary Combustion", Progress Astronautics and Aeronautics, Vol. 15, no. 1, 1964, p 485-492. https://doi.org/10.1016/B978-1-4832-2730-6.50025-7. (accessed 30 March, 2023)

[23] Whitmore, S. A. (n.d.). *Lecture 3.1: Introduction to hybrid rockets - utah state university*. (n.d.). Retrieved April 30, 2023, from http://mae-nas.eng.usu.edu/MAE_6530_Web/New_Course/Section3/section3.1.pdf

[24] Sutton, G. P. (2016, December 27). *Rocket Propulsion Elements*. Google Books. Retrieved April 30, 2023, from https://books.google.com/books/about/Rocket_Propulsion_Elements.html?id=XwSRDQAAQBAJ

[25] Zilliac, G., and Karabeyoglu, A., "Hybrid Rocket Fuel Regression Rate Data and Modeling," AIAA-2006-4504, AIAA/ASME/SAE/ASEE 42nd Joint Propulsion Conference, 9-12 July 2006, Sacramento CA, https://doi.org/10.2514/6.2006-4504. (accessed 30 March, 2023)

[26] Messineo, J., & Shimada, T. (2019). Theoretical investigation on feedback control of hybrid rocket engines. *Aerospace, 6*(6), 65. https://doi.org/10.3390/aerospace6060065

[27] Whitmore, S. A., Walker, S. D., Merkley, D. P., and Sobbi, M. "High Regression Rate Hybrid Rocket Fuel Grains with Helical Port Structures", Journal of Propulsion and Power, Vol. 31, No. 6 (2015), pp. 1727- 1738. http://dx.doi.org/10.2514/1.B35615

[28] *Engineering model for hybrid fuel regression rate amplification using ...* (n.d.). Retrieved April 30, 2023, from https://arc.aiaa.org/doi/10.2514/1.B36208

[29] Whitmore, S. A., Merkley, D. P., & Inkley, N. R. (2014). Development of a power efficient, restart-capable arc ignitor for Hybrid Rockets. *50th*

AIAA/ASME/SAE/ASEE Joint Propulsion Conference. https://doi.org/10.2514/6.2014-3949

[30] *Boron nitride*. Precision Ceramics. (2024, January 5). https://precision-ceramics.com/materials/boron-nitride/

[31] *The Online Materials Information Resource*. MatWeb. (n.d.). https://www.matweb.com/search/DataSheet.aspx?MatGUID=3f64b985402445c0a5af911135909344&ckck=1

[32] *Measurement of fluid flow using small bore precision orifice meters: ASME MFC-14M-2003*. (2003). . ASME.

[33] NIST. (n.d.). https://www.nist.gov/system/files/documents/srd/jpcrd423.pdf

[34] Whitmore, S. A. (n.d.). *Injector Notes*. MAE 6530 - Propulsion Systems II Lecture Notes. http://mae-nas.eng.usu.edu/MAE_6530_Web/New_Course/Section3/section.3.3.1.pdf

[35] Frischkorn, Cara, "In-Situ Optical Measurements of High Temperature Combustion Plumes" (2023). All Graduate Theses and Dissertations, Fall 2023 to Present. 82. https://digitalcommons.usu.edu/etd2023/82

[36] Anderson, J. D., Modern Compressible Flow, 3rd Edition, New York, McGraw Hill, 2003, 127-187. ISBN-13: 978-0072424430. https://libcat.lib.usu.edu/search/i0070016542. (Accessed 30 November, 2023)

[37] NASA. (n.d.). *Rocket Thrust equations*. NASA. https://www.grc.nasa.gov/www/k-12/airplane/rktthsum.html

[38] NASA. (n.d.-c). *Specific impulse*. NASA. https://www.grc.nasa.gov/www/k-12/airplane/specimp.html

[39] Coombs, Trevor W., "Development and Testing of an 8-Bit Digitally Throttled Hybrid Rocket Motor" (2024). *All Graduate Theses and Dissertations, Fall 2023 to Present*. 117. https://digitalcommons.usu.edu/etd2023/117

[40] Whitmore, S. A., Borealis, C. I., & Francom, M. W. (n.d.). Minimally-intrusive, dual-band, fiber-optic sensing system for high- enthalpy exhaust plumes. *Not Yet Published*. https://doi.org/10.3934/era.2024xxx